SPECIAL
RELAMPAGO-CACTI
COLLECTION

Environmental Controls on Simulated Deep Moist Convection Initiation Occurring during RELAMPAGO-CACTI

T. CONNOR NELSON,[a,b,c] JAMES MARQUIS,[d,c] JOHN M. PETERS,[e] AND KATJA FRIEDRICH[c]

[a] *Cooperative Institute for Research in the Atmosphere, Colorado State University, Fort Collins, Colorado*
[b] *NOAA/NWS Operations Proving Ground, Kansas City, Missouri*
[c] *Department of Atmospheric and Oceanic Sciences, University of Colorado Boulder, Boulder, Colorado*
[d] *Pacific Northwest National Laboratory, Richland, Washington*
[e] *Department of Meteorology, U.S. Naval Postgraduate School, Monterey, California*

(Manuscript received 16 August 2021, in final form 18 March 2022)

ABSTRACT: This study synthesizes the results of 13 high-resolution simulations of deep convective updrafts forming over idealized terrain using environments observed during the RELAMPAGO and CACTI field projects. Using composite soundings from multiple observed cases, and variations upon them, we explore the sensitivity of updraft properties (e.g., size, buoyancy, and vertical pressure gradient forces) to influences of environmental relative humidity, wind shear, and mesoscale orographic forcing that support or suppress deep convection initiation (CI). Emphasis is placed on differentiating physical processes affecting the development of updrafts (e.g., entrainment-driven dilution of updrafts) in environments typifying observed successful and null (i.e., no CI despite affirmative operational forecasts) CI events. Thermally induced mesoscale orographic lift favors the production of deep updrafts originating from ~1- to 2-km-wide boundary layer thermals. Simulations without terrain forcing required much larger (~5-km-wide) thermals to yield precipitating convection. CI outcome was quite sensitive to environmental relative humidity; updrafts with increased buoyancy, depth, and intensity thrived in otherwise inhospitable environments by simply increasing the free-tropospheric relative humidity. This implicates the entrainment of free-tropospheric air into updrafts as a prominent governor of CI, consistent with previous studies. Sensitivity of CI to the environmental wind is manifested by 1) low-level flow affecting the strength and depth of mesoscale convergence along the terrain, and 2) clouds encountering updraft-suppressing pressure gradient forces while interacting with vertical wind shear in the free troposphere. Among the ensemble of thermals occurring in each simulation, the widest deep updrafts in each simulation were the most sensitive to environmental influences.

KEYWORDS: Deep convection; Convective storms; Mesoscale processes; Storm environments; Idealized models; Mesoscale models

1. Introduction

The growth of shallow convective clouds into deeper precipitating storms, often referred to as deep moist convection initiation (or "CI") is a challenging process to represent in numerical weather prediction and climate models, and presents a notoriously difficult weather forecasting problem. Forecast uncertainties stem from the dependency of CI on complex processes that interact across a wide range of $O(10^{-1}–10^{2})$ km scales (Xue and Martin 2006; Duda and Gallus 2013; Moser and Lasher-Trapp 2017). Due to this wide range of scales, operational mesoscale numerical weather prediction must rely on a mix of cumulus, turbulence, microphysics, and convective boundary layer parameterization schemes to represent much of the CI process acting on subgrid scales (e.g., Davis et al. 2003; Trier et al. 2004, 2011; Wilson and Roberts 2006; Weisman et al. 2008; Duda and Gallus 2013; Rousseau-Rizzi et al. 2017).

Many recent studies of large-eddy simulation (LES) show that processes critical to CI are underresolved by typical operational mesoscale forecast models. For example, cumulus and cumulonimbus clouds are composed of discrete, positively buoyant thermals that interact with the environment through entrainment that occurs on scales that are typically smaller than the lower resolution limit of mesoscale models (French et al. 1999; Damiani et al. 2006; Houston and Niyogi 2007; Varble et al. 2014; Moser and Lasher-Trapp 2017; Rousseau-Rizzi et al. 2017; Morrison 2017; Hernandez-Deckers and Sherwood 2016, 2018; Peters et al. 2020). CI is strongly influenced by the entrainment-driven dilution of core updraft buoyancy (Zhao and Austin 2005; Romps 2010; De Rooy et al. 2013; Morrison 2017; Hernandez-Deckers and Sherwood 2016, 2018; Morrison et al. 2020; Peters et al. 2020). All other conditions being equal, the rate at which buoyancy is diluted is inversely proportional to the width of the buoyant thermal

Corresponding author: T. Connor Nelson, tconnorn@colostate.edu

DOI: 10.1175/JAS-D-21-0226.1

(Morrison 2017; Lecoanet and Jeevanjee 2019; Morrison et al. 2020; Peters et al. 2020). Thus, entrainment will tend to inhibit CI associated with narrower clouds to a greater extent than with wider clouds. Morrison et al. (2021) and Peters et al. (2022a,b) argue that the width of the region of subcloud ascent that triggers a cloud, and ultimately influences a cloud's width, is a critical factor in determining whether or not CI will occur.

Orography often promotes CI through the production of subcloud updrafts via solar heating of elevated terrain and "mechanically forced" updrafts by the mesoscale flow impinging on it (e.g., Kirshbaum et al. 2018). These factors are likely to modulate the size of updrafts within the planetary boundary layer, and by extension, the likelihood of CI (Marquis et al. 2021). Using uniform horizontal wind profiles in two-dimensional simulations, Kirshbaum (2011) illustrate that orographic CI is sensitive the magnitude of the cross-terrain flow, owing to its ability to disrupt the convergence of boundary layer buoyancy near a mountain peak that is achieved by thermally induced anabatic flow. Other environmental factors influencing CI include relative humidity (RH) and vertical shear of the horizontal wind in the "free troposphere" (i.e., the layer of the troposphere located above the boundary layer). Recent modeling studies show that the effects of entrainment are more detrimental when free-tropospheric RH is relatively small (Morrison 2016; Morrison et al. 2020, 2021; Peters et al. 2020). Together, RH and the width of the subcloud updraft determine whether or not CI occurred in the idealized simulations of Morrison et al. (2021). Some studies have implied that shear may directly modify turbulent entrainment processes (e.g., Zhao and Austin 2005; Wang et al. 2008, 2012), while others implicate downward-pointing vertical pressure gradient forces resulting from shear–updraft dynamic interactions that decelerate ascending thermals and stifle deepening clouds (the so-called shear-suppression effect) (Peters et al. 2019, 2022a,b). However, the relative roles of RH, wind shear effects, and terrain–flow interactions play on the growth of cloud-scale updrafts in observed environments are not well understood.

The Remote Sensing of Electrification, Lightning, and Mesoscale/Microscale Processes with Adaptive Ground Observations (RELAMPAGO; Nesbitt et al. 2021) project, and the companion Cloud, Aerosol, and Complex Terrain Interactions (CACTI; Varble et al. 2021) field campaign aimed to better understand the interaction between the mesoscale environment and complex terrain producing CI in central Argentina. These campaigns collected numerous radiosonde soundings within 10–30 km of growing congestus along the Sierras de Córdoba (SDC) range, yielding a large sample of observed near-cloud ambient conditions ideal for testing environmental influences upon CI (Schumacher et al. 2021). In a companion study to this one, Nelson et al. (2021) used the RELAMPAGO-CACTI radiosonde sounding dataset to statistically differentiate near-cloud environments associated with a variety of CI outcomes, ranging from environments yielding sustained storms to null events (i.e., no CI despite affirmative operational forecasts from 3- to 4-km-horizontal-resolution convective-allowing models). Evaluation of many common operational environmental metrics across cases revealed that null events often contained better convective potential than environments supporting observed CI. However, lower values of free-tropospheric RH in null environments led Nelson et al. (2021) to hypothesize that entrainment of free-tropospheric air into cloudy updrafts was a prominent factor differentiating CI outcome.

In this study, we combine the RELAMPAGO-CACTI sounding database with high-resolution three-dimensional simulations to examine updraft–environment interactions governing orographic CI. This work provides numerical evidence of physical processes supporting hypotheses related to free-tropospheric RH based on purely observational analysis of the RELAMPAGO-CACTI soundings by Nelson et al. (2021). Further, it builds upon pivotal cloud-scale simulations of orographic CI (e.g., Kirshbaum and Durran 2004; Kirshbaum 2011, 2013; Kirshbaum et al. 2018; Hagen et al. 2011; Soderholm et al. 2014; Singh et al. 2022) and other theoretical or LES treatments of updraft–environment interactions (e.g., Moser and Lasher-Trapp 2017; Peters et al. 2019, 2022a,b; Rousseau-Rizzi et al. 2017; Morrison et al. 2020, 2021; Hernandez-Deckers and Sherwood 2016, 2018; Varble et al. 2014) by considering the influences of vertical shear of the horizontal wind upon CI. In doing so, we relate the sensitivity of CI to both subcloud mesoscale ascent that is affected by the terrain-relative low-level wind (e.g., Kirshbaum 2011) and possible shear-suppression effects epitomized by dynamically induced vertical pressure gradient accelerations (VPGAs; e.g., Peters et al. 2019, 2022a,b). Our examination of various environmental profiles contextualizes the sensitivities in which CI might have occurred in observed null events had certain environmental conditions been met (and vice versa) by comparing relative differences in important physical processes governing updraft growth (e.g., entrainment of environmental air into the cloudy updrafts and dynamically induced vertical pressure gradient forces) occurring among an ensemble of simulations.

The manuscript organization is as follows: section 2 discusses the model configurations and general experimental design, section 3 and 4 analyze the sensitivity of our results to differing observed and modified environmental conditions, and to model assumptions. The results are discussed in the context of past studies in section 5. Our key findings are summarized in section 6.

2. Methods

We performed 13 high-resolution three-dimensional simulations using the Cloud Model 1 (CM1; Bryan and Fritsch 2002) version 19.8. The CM1 configurations used in this study are summarized in Table 1. The majority of our simulations used a uniform horizontal grid spacing of 250 m and a vertical grid spacing of 125 m over a $270 \times 360 \times 13$ km^3 static domain with periodic lateral boundary conditions. Though these dimensions are on the cusp of cloud-scale resolution, a horizontal grid spacing of 250 m has been shown to be adequate to resolve the inertial subrange and for LES subgrid-scale closures to sufficiently perform as designed (Bryan et al. 2003; Lebo and Morrison 2015), while preserving computational

TABLE 1. Summary of CM1 specifications and configurations used.

Specification	Value
CM1 version	19.8
Model resolution (x, y, z)	$0.25 \times 0.25 \times 0.125$ km^3
Domain size (x, y, z)	$270 \times 360 \times 13$ km^3
Grid points (x, y, z)	$1080 \times 1440 \times 103$
Time step	Adaptive 1 s
Radiation (LW, SW)	WRF-RRTMG (Iacono et al. 2008)
Land-use type	WRF-grassland, soil moisture availability = 0.5
Microphysics	Two-moment Morrison (Morrison et al. 2005)
Terrain	Idealized SDC
Lateral boundary conditions	Periodic
Surface boundary conditions	Semislip and Monin–Obukhov (from WRF)
Top boundary conditions	Rigid free slip with Rayleigh damper (>10 km)
Integration time	2 h
Subgrid turbulence	TKE, LES
Coriolis acceleration	Off
Boundary layer physics	—
Cumulus parameterization	None

resources for a number of environmental sensitivity simulations. We accounted for subgrid turbulence with the TKE and LES parameterizations available in CM1. Our rationale for the domain vertical extent is that we are focusing on convection relatively early in the life cycle, where it is limited to ~9–11 km deep and when complex gravity waves and reflections off of the top of the domain are expected to be minimal.

We prescribed a rigid free slip condition at the model top and a Rayleigh damper for altitudes above 10 km with a coefficient of 3.33×10^{-3} s^{-1} to limit artifacts of waves. Simulations were run with an adaptive time step (initially 1 s) for 2 h, and output was saved at 1-min frequency in all but select analyses described in section 3, for which output was saved every 5 s. The surface was semislip with surface exchange coefficients based upon the land-use type. The land use was specified as grassland [from Weather Research and Forecasting (WRF) Model parameterizations] with a soil moisture availability of 0.5 (Nowotarski et al. 2014; Mulholland et al. 2020). Surface fluxes of heat, moisture, and momentum were parameterized using the summertime WRF-grassland surface model and Monin–Obukhov similarity theory surface model (Grell et al. 1994) following Mulholland et al. (2020). The initial values for the shallow and deep soil temperatures were 299 and 297 K, which are the default values for CM1. Coriolis accelerations were neglected and no boundary layer parameterizations were prescribed. We used the two-moment Morrison microphysics scheme (Morrison et al. 2005).

The majority of our simulations included longwave and shortwave radiation, surface fluxes, and idealized terrain approximating that of the SDC near where the environmental conditions were observed. We prescribed an idealized terrain elevation profile (Z_s; where s denotes the model surface) consisting of an elliptical-Gaussian mountain similar to Mulholland et al. (2020) and Dörnbrack et al. (2005),

$$Z_s(x, y) = h \times \left\{ \left[1 + \left(\frac{X}{a} \right)^2 \right]^{-1.5} \right\}, \quad (1)$$

$$X = \sqrt{(x + \gamma x_{\max})^2 + \beta[(\alpha y + \varphi y_{\max})^2]}, \quad (2)$$

where h is the maximum terrain height[1] (1.25 km), $x_{\max}$ and $y_{\max}$ are the dimensions of the model domain in the x and y directions (270, 360 km, respectively), a is the horizontal half-width of the ridgeline (15 km), X is a "stretching parameter," γ and φ are factors prescribing the x and y positions of the center of the terrain relative to the model domain center (0.65, 0.10, respectively), and β and α are stretching coefficients for the entire terrain feature in the north–south and east–west directions (0.15, 0.40, respectively). We called the WRF-RRTMG radiation scheme (Iacono et al. 2008) every 15 min, initialized at 1600 UTC 6 November at −31.97° latitude, −64.68° longitude, which was the mean location and time for the soundings comprising the composite soundings. Results from several experiments utilizing this model configuration are analyzed in section 3, while a small subset of sensitivity experiments that exclude terrain, surface fluxes, and radiation are discussed in section 4.

The environmental conditions in our domain were initialized with horizontally homogeneous base-state variables (potential temperature, surface pressure, wind) derived from RELAMPAGO-CACTI composite soundings generated by Nelson et al. (2021). In that study, the onset of low-level radar reflectivity from a convective cloud was used to define the time and location of CI to assign an appropriate sounding from the radiosonde array to characterize the near-cloud environment (occurring within 30 km and 30 min of the surface precipitation). Each composite sounding represents mean near-cloud environments containing 1) radar-observed initiation of sustained precipitating convection producing near-surface reflectivity > 35 dBZ for at least 20 consecutive min (i.e., sustained CI events, hereafter "SCI"; Fig. 1a), 2) radar-detected weak and short-lived convection with near-surface reflectivity < 35 dBZ or precipitation persisting less than 20 consecutive min (i.e., poorly sustained CI events, hereafter referred to as "Fail" events; Fig. 1b), and 3) no observed precipitating convection despite forecasts of CI from an ensemble of convection-allowing WRF simulations (hereafter "Null" events; Fig. 1c). The composite SCI, Fail, and Null soundings are averages of 13, 19, and 12 events, respectively. Soundings comprising each composite were collected in regions of upslope flow along the lee sides of the SDC and Andes Mountains between 1500 and 2000 UTC (77% were between 1500 and 1700 UTC). For simplicity of naming convention, all heights referenced from the mean

[1] The value of h was prescribed based on the relative difference of the true peak elevation of the SDC range and the mean height above sea level of the radiosonde launch sites used in this study (z ~ 1 km above mean sea level).

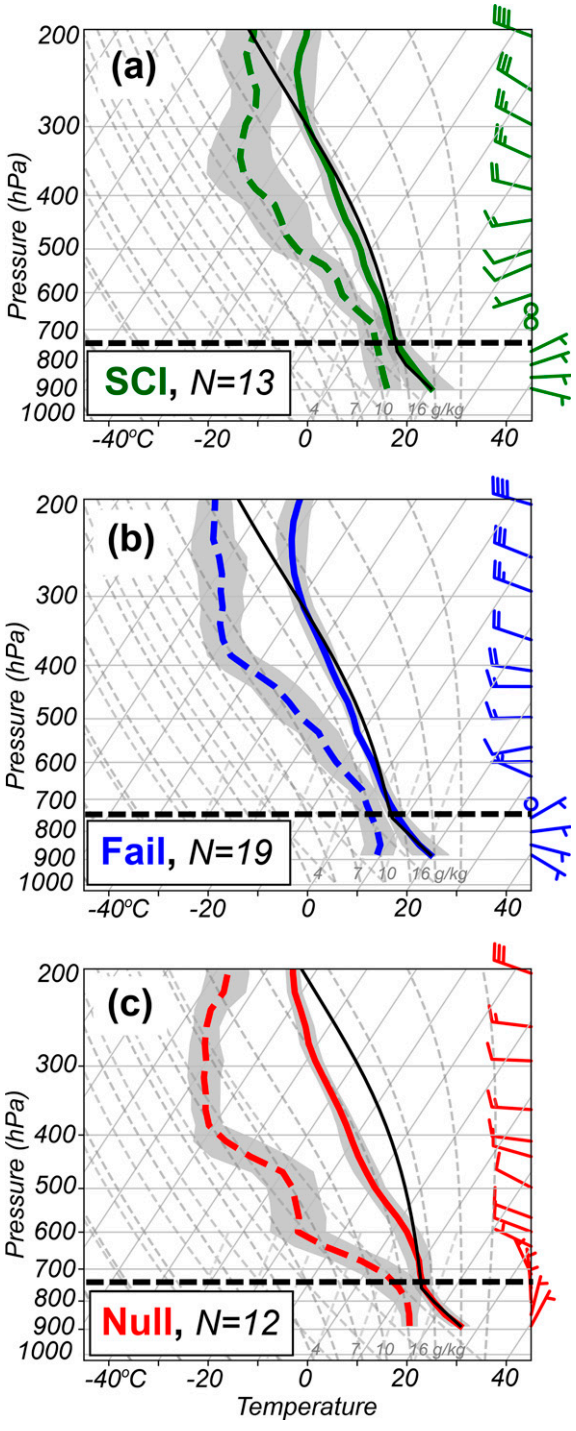

FIG. 1. Mean soundings representative of (a) SCI (green), (b) Fail (blue), and (c) Null (red) events, adapted from Nelson et al. (2021). The mean temperature is the solid line, the mean dewpoint temperature is the dashed line, and the mean surface-based parcel is the solid black line. The mean horizontal wind for each event type is plotted as wind barbs on the right side of each panel. The horizontal dashed line in all panels denotes the approximate peak terrain height. The total number of soundings (N) and the standard deviation for each sounding (gray shading) is also provided.

radiosonde launch height will hereafter be referred to as "above mean sea level" in the model domain (MSL).

As noted by Nelson et al. (2021), Fail events often occurred 1–2 h prior to SCI events, with only subtle differences in the environmental profiles. Composite environments supporting SCI and Fail events have similar convective available potential energy (CAPE; 250–350 J kg^{-1}), convective inhibition (CIN; ~45–50 J kg^{-1}), level of free convection (LFC; ~1.7–1.9 km MSL) for lifted surface parcels, with slightly different equilibrium levels (ELs; 7.8 km MSL for Fail and 8.6 km MSL for SCI), and similar free-tropospheric RH (mean RH of ~28%) (Figs. 1a,b). The Null environment has greater CAPE (~1100 J kg^{-1}), slightly less CIN (33 J kg^{-1}), comparable lifting condensation level (LCL; ~1.2 km MSL), slightly lower LFC (~1.3 km above launch height), higher EL (~10.8 km MSL), and drier free-tropospheric RH (mean RH of ~10%) (Fig. 1c).[2] Though we assume horizontal homogeneity, our three-dimensional model domain affords an evaluation of CI by complex three-dimensional mesoscale effects owing to the presence of both terrain-parallel and cross-terrain wind components.

CI can be defined by numerous metrics representing processes associated with the initial release of CAPE by parcels reaching their LFC, a cumulus cloud achieving a specified depth threshold, the initial formation of in-cloud precipitation, etc. For simplicity, and to parallel many past observational studies using radar observations, we define the occurrence of CI in our simulations to be when precipitation is first detected at the surface. Our overall modeling strategy was designed to examine sensitivities of CI to the interaction between storm-scale updrafts and the near-cloud environment. Several studies indicate the importance of a variety of meso-beta-scale phenomena to orographic CI such as the presence of a low-level jet, complex terrain structure, or leeside flow convergence zones (e.g., Banta 1984; Banta and Schaaf 1987; Behrendt et al. 2011; Hagen et al. 2011; Kirshbaum and Wang 2014; Soderholm et al. 2014; Mulholland et al. 2020; Marquis et al. 2021; Singh et al. 2022). Though our use of soundings synthesizing several convective event types is similar to other deep convective modeling studies (e.g., Coffer and Parker 2017), it is worth noting that CI may be sensitive to specific details of the environments in individual cases (e.g., the three-dimensional variability of boundary layer properties, capping inversions, sharp wind shear layers). While our soundings smooth out some of the fine-scale details of such atmospheric profiles (e.g., fine-scale vertical variability in the temperature or dewpoint temperature profiles), they exhibit generally low sounding-to-sounding variance (as shown by the gray shading in Fig. 1) and, therefore, can be reasonably used to diagnose the impact of salient environmental features, like free-tropospheric moisture or wind shear on the CI process.

We assess updraft, buoyancy {as defined in CM1, $B \equiv g[\theta'/\theta_0 + (R_v/R_d - 1)r'_v - r_c]$}, and VPGAs $[(1/\rho)(\partial p'/\partial z)]$

[2] The specific values reported here for the SCI, Fail, and Null soundings are different from those reported by Nelson et al. (2021), because the values referenced here are for parcels lifted from the composite soundings themselves rather than the mean of individual values for each sounding.

acting on the updraft among these different environments during the CI period in our simulations. Other physical processes may be significant in the vertical momentum budget (e.g., entrainment of updraft from momentum and mass exchange; Peters et al. 2019). We qualitatively estimated entrainment-driven dilution of thermals with free-tropospheric air through the cloud column by tracking the three-dimensional concentration of air from the subcloud layer with a passive tracer field initialized at model $t = 0$ with a value of 1.0 kg kg^{-1} within the lowest 2 km MSL of the atmosphere and 0.0 kg kg^{-1} above it. This tracer layer was chosen to be comparable to the depth of the sounding-estimated boundary layer depth, ~1 km as noted by Nelson et al. (2021), near the terrain peak where CI occurs and ensures that air above the LFC is initialized with a passive tracer value of zero. We examined vertical gradients of the passive tracer as a qualitative metric for dilution of thermals by free-tropospheric air. We opted for this metric over a more direct calculation of entrainment or dilution (e.g., parcel or thermal trajectory calculations; Hernandez-Deckers and Sherwood 2018) because of the computational cost of performance over several experiments. While our model grid spacing may not fully resolve certain turbulence scales associated with deep convection, we believe that the turbulent processes do scale appropriately to ~250 m or less because our resolution is at or well below the critical thresholds noted by Lebo and Morrison (2015) for relatively low sensitivity in convective morphology and entrainment/detrainment processes. Our analysis focuses on the relative differences of these processes across varying background meteorological conditions to explore the impact of each environment on cloud growth.

Based on several studies cited in the introduction, it is highly informative to quantify the width of cloudy updrafts in our experiments to best understand the CI process. To do so, we tracked (in space and time) ensembles of individual moist thermals comprising updrafts occurring in each simulation within ±15 min of the onset of surface precipitation. To do so, we used an algorithm similar to one used by Peters et al. (2019) that leverages prior methods by Sherwood et al. (2013) and Hernandez-Deckers and Sherwood (2016). At each output time (saved every 5 s during this 30-min window), we identified local maxima in vertical velocity (w) maxima that exceeds 3 m s^{-1} within 500 m of each grid point in all Cartesian directions. Each detected maxima was labeled as a "thermal center candidate" (TCC), whose center is tracked forward and backward in time by matching it with the closest TCC at adjacent time steps within a three-dimensional cone predicted by the expected ascent rate [see Peters et al. (2019) for more details]. If the algorithm yielded the same matching TCCs going forward and backward in time, then they were considered to be part of the same thermal track. Resulting thermal tracks with less than three data points were removed. The thermal volume was defined as a spherical region centered at the TCC whose average w is equal to that of the TCC's ascent rate. For each model run, we cataloged updraft size (mean and 90th percentile thermal width) among ensembles occurring in each simulation and compute vertical volumetric mass flux (M; kg km s^{-1}), defined at a given height as

$$M = \sum WV\rho, \tag{3}$$

where $\sum$ represents a sum over all thermals at a given height, W is the thermal's ascent rate, ρ is density, and V is the thermal volume.

3. Terrain-inclusive simulations

A simulation employing the Null base-state environment (Fig. 1c) demonstrates that an anabatic mesoscale orographic upslope flow and a deepening dry convective boundary layer begin to develop within 20 min of model initialization (Figs. 2a,d). By t = 60 min, +1–2-K magnitude thermal eddies that scale with the depth of the boundary layer (~1 km-deep) consolidate near the terrain peak, yielding an approximately 5-km-wide swath of horizontal wind convergence[3] (Figs. 2c,f and 3b). As mentioned in section 2, we initialize our simulations with composite soundings that represent afternoon near-cloud conditions; thus, the rapid development of boundary layer and orographic circulations is likely a result of these environments already showing the thermodynamic effects of several hours of daytime insolation destabilizing the lower atmosphere by the start of model forecasts. Regardless of this rapid development, a thermally forced orographic circulation resembling past studies (e.g., Demko and Geerts 2010; Kirshbaum 2011, 2013, 2017, 2020; Kirshbaum and Wang 2014; Soderholm et al. 2014; Mulholland et al. 2020) provides a mesoscale region of convergence and lift, through which humid boundary layer thermals ascend into the free troposphere to produce deep convective clouds. We make use of these conditions rather than relying on a more gradual evolution of the boundary layer over a longer forecast period initialized with a morning sounding (e.g., Kirshbaum 2011) to prevent forecasted near-cloud environments from potentially diverging from the observed conditions that we aimed to interrogate. As described below, both observed CI and Null outcomes are qualitatively reproduced by our simulations.

a. *Base SCI, Fail, and Null environments*

Our first set of simulations applied the horizontally homogeneous environmental state composed of the composite SCI, Fail, and Null base soundings (Fig. 1). This series of simulations produces precipitation qualitatively resembling the span of observed outcomes during RELAMPAGO-CACTI (Fig. 4). Widespread and sustained precipitation first reaches the surface at t ~ 58 min in the SCI and Fail environments (Figs. 4a,b, Figs. 5a,d, and 6a). Although surface precipitation is realized in the base Null run, it is much more isolated, less intense, and first occurs approximately 17 min later than in the base SCI and Fail runs (Figs. 4c, 5g, and Figs. 6b). Storms forming in the Fail environment are only subtly weaker and less widespread than their SCI counterparts, with similar convective structure and evolution (Figs. 4a,b and 5a–f). It is

[3] Convergence is calculated from the two-dimensional divergence field computed in CM1 in terrain following coordinates, remapped to a Cartesian grid.

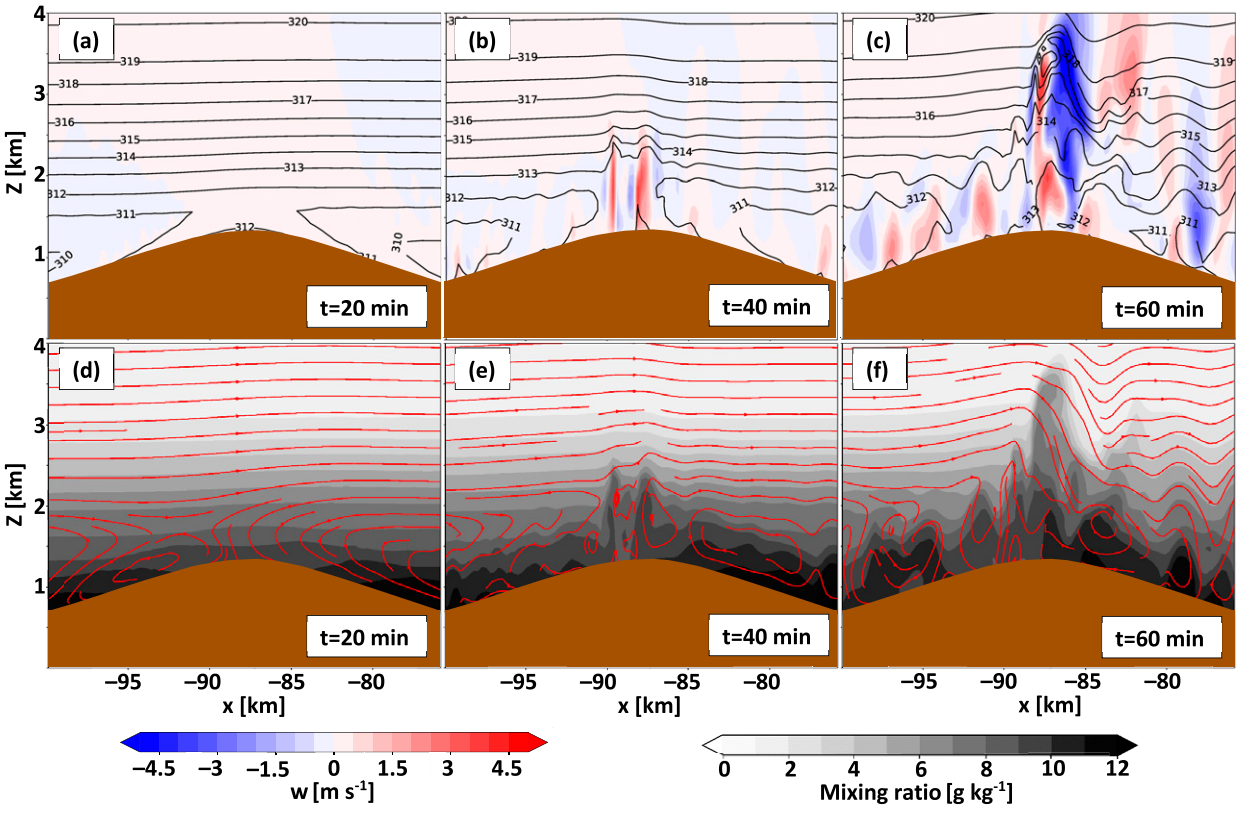

FIG. 2. Evolution of the orographic circulation using idealized terrain, radiation, and surface fluxes. (a)–(c) The evolution of vertical velocity (m s^{-1}, shaded) and potential temperature (K, contours). (d)–(f) The evolution of mixing ratio (g kg^{-1}, shaded) and streamlines (red).

possible that representation errors in the composite soundings, and/or subtle forecast errors of in-cloud microphysical processes or mesoscale and boundary layer circulations by our model assumptions reconcile the differences between observed SCI and Fail events. Due to the similarities between the SCI and Fail simulations, our remaining analysis compares processes occurring across just the base SCI and Null environments.

In both the SCI and Null simulations, boundary layer parcels ascend to their LFC within the mesoscale orographically induced updraft. This updraft is displaced to the west of the terrain ridgeline in the SCI simulation, consistent with advection by the low-level easterly upslope flow (e.g., Kirshbaum and Durran 2004; Kirshbaum 2011, 2013; Wang et al. 2016) (Figs. 5a–c,g–i). Eventually, a chain of rising buoyant thermals produces precipitation rates in excess of 60 mm h^{-1} in the SCI run (e.g., Fig. 6a). The mesoscale updraft in the Null simulation is located nearer to the ridgeline (or just east of it) because of a weaker cross-terrain flow at low levels (Kirshbaum 2013; Soderholm et al. 2014), but is narrower and shallower than the SCI run, with a weaker orographic circulation and surface convergence (Figs. 3a,b and 5b,h). Shallower convection and smaller precipitation rates (< 10 mm h^{-1}) are produced in the Null simulations than in the SCI simulations despite similar peak cloud updraft strengths (Figs. 5b,e,h and 6a,b).

The mean diameter of all tracked thermals for both the SCI and Null simulations is ~1700 and ~1600 m, respectively (Fig. 7a). Although the mean width of all tracked thermals is only slightly larger in the SCI than in the Null simulations, the diameters of widest updrafts (e.g., 90th percentile in radius among the ensemble of updrafts produced in each simulation) in the SCI run are at least 800 m greater than in the Null run (maximum difference is ~1000 m at $z = 3$ km above the terrain peak; hereafter "ATP";[4] Fig. 7a). The ensemble of thermals produced in the SCI simulation has a significantly larger domain-averaged volume mass flux than Null thermals due to both the greater size and more numerous updrafts (Fig. 7b). Both SCI and Null updrafts experience similar buoyancy and VPGA below 3 km AGL (Figs. 8a,b and 9a,b). Above this altitude, the Null updrafts contain greater buoyancy than the SCI updrafts because of greater CAPE present in the Null environment (Figs. 8a,b). However, Null updrafts experience much more significant downward-oriented VPGAs than the SCI updrafts (Figs. 9a,b), an expected consequence of an increased contribution from the

[4] Note that ATP is different from "above ground level" (AGL), as ATP is height relative to a constant reference point ($z = 1.25$ km MSL) and AGL is height above the ground, which is a nonconstant height. When at $h = 1.25$ km MSL, then AGL is the same as ATP.

buoyancy perturbation pressure (e.g., Markowski and Richardson 2010; Morrison 2016;Peters et al. 2019).[5]

The net concentration of boundary layer air transported into the free troposphere per height within updrafts in the Null simulation is less than for the SCI simulation, and evaporation rate[6] of cloudy air is much higher in the Null case, because the free-tropospheric RH is considerably lower (e.g., z = 4–8 km AGL in Figs. 10a,b and 11a). Entrainment-driven dilution of buoyancy within the Null clouds may be particularly effective owing to their largest updrafts being smaller and weaker surface convergence supporting them than in the SCI environment (Figs. 3 and 7a). Updrafts in the Null simulation fall quite short of their EL that is predicted by parcel theory, likely because of strong dilution of in-cloud buoyancy and adverse VPGAs aloft (Figs. 8b, Figs. 9b, and 11b). Though the SCI cloud depths reach a similar altitude and achieve less maximum positive buoyancy, they more closely accomplish their maximum altitude predicted by parcel theory in the presence of milder opposing VPGAs and less entrainment-driven dilution of buoyancy (corresponding to a more humid free troposphere) (Figs. 6a, Figs. 8a, and 9a). Indeed, the SCI updrafts experience less adverse VPGA relative to their buoyancy despite the SCI simulation having stronger environmental wind shear than the Null simulation (Fig. 11b).[7]

b. *Relative humidity experiment*

To test a hypothesis posed by Nelson et al. (2021), we performed an experiment examining the sensitivity of CI outcome to the observed moisture conditions. We employed the same model and base-state configuration as in section 3a; however, we modified the base SCI and Null environments by swapping their dewpoint depression profiles. In doing so, we compute a new dewpoint temperature profile by retaining the base-state temperature profile and subtracting the dewpoint depression from the counterpart environment (SCI or Null). This has the effect of moistening the free troposphere in the Null thermodynamic environment and drying it in the SCI environment (Fig. 12). We posed this experiment to test if CI could have occurred in the observed Null environments if it had a similar moisture profile as that in the observed SCI environments. For naming convention, we refer to the swapped humidity profile simulations as "moistened Null" and "dried SCI." However, we note that simply swapping these dewpoint depression (i.e., moisture) profiles results in a subtle drying of the Null boundary layer and moistening of the SCI boundary layer, which alters values of CAPE, CIN, and other metrics relevant to CI for low-level mean-layer (ML) parcels (Fig. 12). The ramifications of these changes are discussed below.

The dried SCI environment produces shorter updrafts (by ~2 km), dramatically reduced precipitation rates (by 50% or more), and cells that are more isolated than in the base SCI experiment (cf. Figs. 6a,c). Further, precipitation formation is delayed, beginning at t = 100 min versus t = 60 min in the base SCI run (Figs. 6a,c). In contrast, the moistened Null environment produces convection akin to the base SCI run, but with deeper and stronger updrafts, and only slightly delayed and weaker precipitation rates than in the base Null or base SCI environments (cf. Figs. 6a,d). Mean updraft width in the moist environments (base SCI and moistened Null) is not significantly different from the dry counterpart environments (dried SCI and base Null), and the largest (e.g., 90th percentile radius) updrafts are only slightly wider in the moistened Null than the base Null simulations (by less than 200–400 m in diameter), yet volume mass flux is larger in the moist simulations owing to more numerous and stronger updrafts (Fig. 7).

Both of the moist simulations retain a larger concentration of in-cloud passive boundary layer air tracer per updraft depth than the dry environments, implying larger net entrainment of free-tropospheric air into the cloud column of the dry environment simulations (cf. Figs. 10a–d and 11a). Mean thermal buoyancy is consistently more positive in the moist environments than in the dry ones, likely a result of reduced buoyancy dilution associated with overall less evaporation of cloudy air and comparatively more humid free-tropospheric air (cf. Figs. 8a–d and 10a–d). As mentioned above, a ML parcel lifted in the dried SCI environment, has slightly greater CAPE and lower CIN than the base SCI environment, while a ML parcel lifted in the moistened Null profile has slightly less CAPE and more CIN than the base Null environment (Fig. 12). Because these ML parcel CAPE and CIN changes might be expected to lessen buoyancy of low-level updrafts produced in the moistened Null run and promote them in the dried SCI run (the opposite outcome of what is simulated), these results suggest that updraft buoyancy characteristics are quite significantly altered by dilution with their free-tropospheric surroundings in these simulations.

There was no alteration of the base-state wind profiles in this experiment, so the magnitude of the low-level orographic convergence near the time of CI is not substantially altered (cf. Figs. 3a–d). As in the base SCI simulation, the moistened Null simulation yields a long-lasting orographically driven mesoscale updraft through which boundary layer thermals ascend into the free troposphere. Whereas, sustained deep updrafts emerging from the orographic circulation do not occur in the dried SCI environment until much later (t = 90–100 min; Fig. 6c). Though the Null environments had slightly greater

[5] Though we might intuitively expect larger downward-oriented pressure gradient forces in the SCI updrafts owing to their relatively large size (Fig. 7a) (e.g., Markowski and Richardson 2010), the total VPGA (shown in Fig. 9) is considerably stronger for the Null updrafts despite their comparatively small width, possibly a result of the Null updrafts having a much higher magnitude of positive buoyancy.

[6] The evaporation rate is computed from components of the potential temperature budget, which is standard output for CM1 using the two-moment Morrison microphysics scheme (Morrison et al. 2005).

[7] Due to the scaling relationship between VPGA and buoyancy resulting from buoyancy pressure gradient accelerations (e.g., Markowski and Richardson 2010; Morrison 2016; Peters et al. 2019), we examined vertical profiles of VPGA normalized by buoyancy for select simulations. In doing so, it allows for better comparison of VPGA effects between runs with different buoyancy strengths.

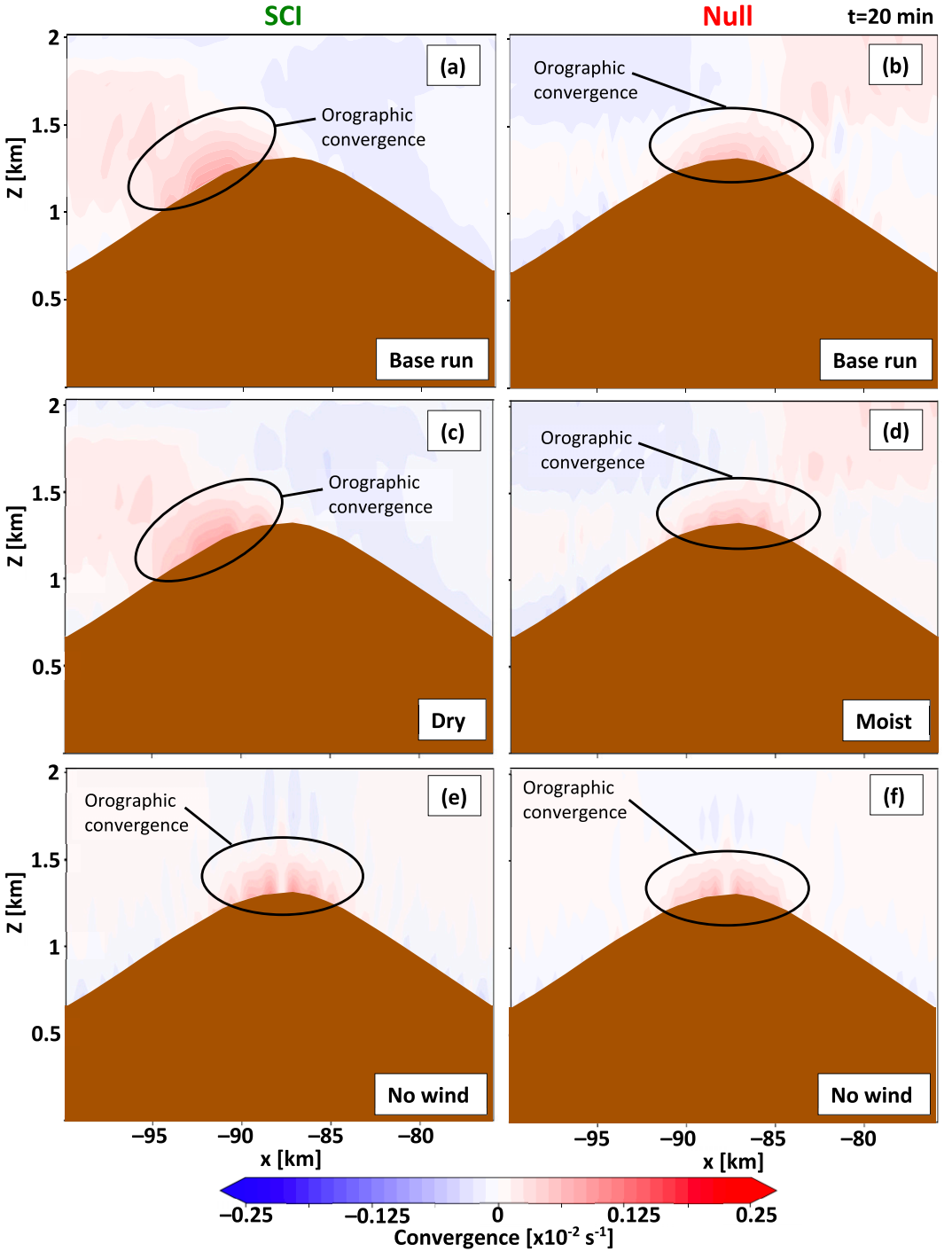

FIG. 3. Convergence (shaded, s^{-1}) at 20 min into the (left) SCI and (right) Null (a),(b) base, (c),(d) dry/moist, and (e),(f) no wind. Convergence (positive values) are shown in red and divergence (negative values) are shown in blue. The E–W cross sections are taken at the same location as those in Fig. 5 (denoted by the thick black lines in Fig. 4).

static stability near the top of the boundary layer, moistening the free troposphere of the base Null profile helps updrafts once they overcome the larger CIN. The moist Null simulation also has a smaller cloud evaporation rate compared to the base Null, suggesting that the negative effects of entrainment are abated when moistening the free troposphere (Figs. 10b,d). Altogether, these results suggest that if the observed Null environments were not as dry, then perhaps deep convection may have been deeper and stronger than in the base SCI environment because of the larger ELs and CAPE.

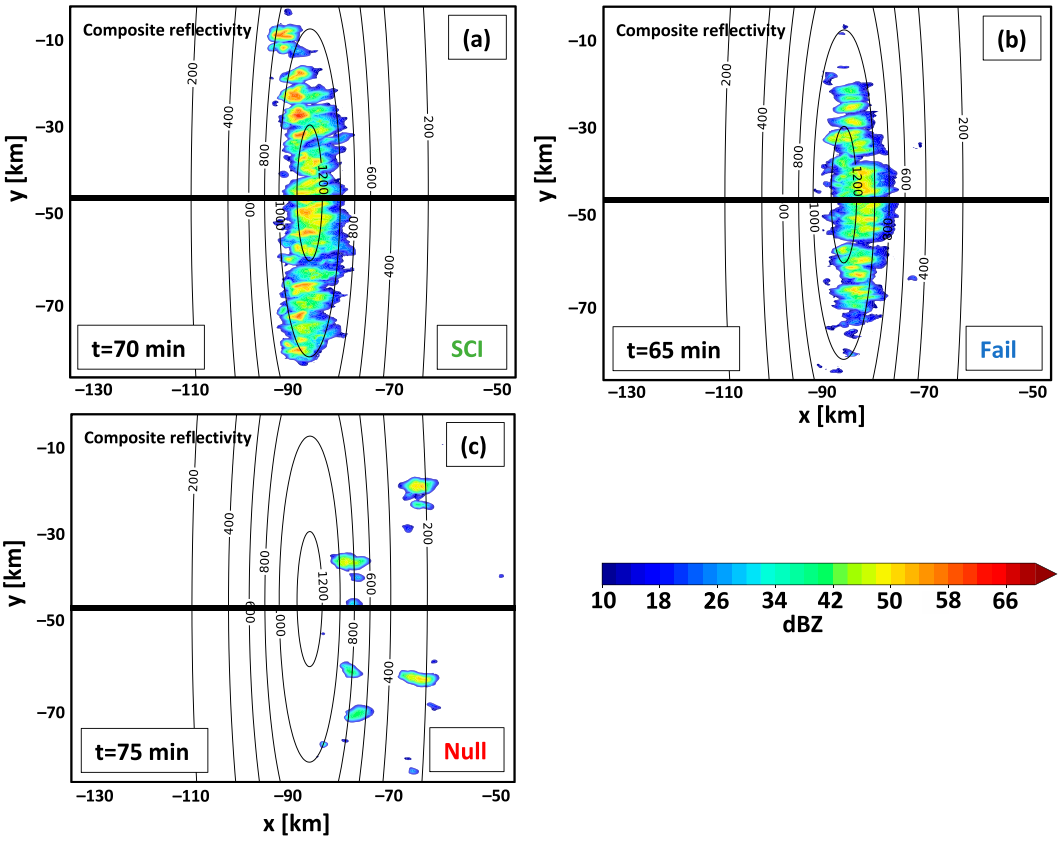

FIG. 4. Composite reflectivity for the (a) SCI, (b) Fail, and (c) Null simulations with idealized terrain, radiation, and surface fluxes. The thick black line denotes the location of E–W cross sections in Fig. 5.

c. Wind variation experiment

To explore the relative effects of the background wind on cloud-scale updraft processes (e.g., suppression of cloud growth from shear-related effects) and the mesoscale orographic circulation, we conducted a variety of sensitivity experiments altering the base SCI and Null wind profiles. With the background wind profile set to zero (i.e., no wind; hereafter "NW"), precipitating convection in the NW SCI environment occurs at approximately the same time and geographical location as in the base SCI run, except with stronger updrafts and a greater precipitation rate (by a factor of ~1.5 and 3, respectively; Figs. 6a,e). Thus, removal of the background low-level easterly wind (and corresponding upslope flow on the east side of the terrain), does not halt the development of convection.

The maximum updraft strength attained in the NW Null environment is diminished between t = 30–65 min relative to the base Null environment, a result of the relatively strong static stability atop the boundary layer that caps the ascent associated with the solenoidal terrain circulation (Figs. 1c, 3, and 5i). Further, this terrain circulation is slightly weaker in the absence of a background mesoscale low-level flow (cf. Figs. 3b,f and 5g–i). However, NW Null peak updrafts are considerably stronger and deeper at $t > 65$ min (> 28 m s^{-1} and 2–4 km, respectively), with more widespread precipitation than the base Null profile and stronger updrafts than in the base or NW SCI runs (Figs. 6a,b,e,f). These stronger updrafts develop partially because by this time there is enough convergence and buoyancy near the terrain peak to reduce the capping inversion, allowing sufficiently developed boundary thermals to enter the free troposphere (e.g., Figs. 2 and 8). The suppressing effect of the cap is not as oppressive early in the base Null run because of the inclusion of background low-level upslope flow. Further, despite having comparable low-level convergence magnitude, the inclusion of wind yields greater elevated convergence (e.g., $z > 1.5$ km MSL) east of the peak in the base Null run compared to the NW Null run (Figs. 3b,f), perhaps analogous to the behavior of convergence in varying wind profiles shown by Hagen et al. (2011). The nature of the orographic flow is significantly different between the base and NW SCI experiments. The area of convergence is shifted eastward to the ridgeline and is shallower in the NW SCI run compared to the base SCI (Figs. 3a,e); though, the depth of convergence AGL is similar. Ultimately, updrafts from both the NW SCI and NW Null simulations reach their Els predicted by parcel theory, unlike their base SCI and Null environment counterparts.

Diameters of the largest thermals (90th percentile) are almost twice as large in the NW Null environment than the base Null environment (by 1.5–2.0 km in diameter; Fig. 7a).

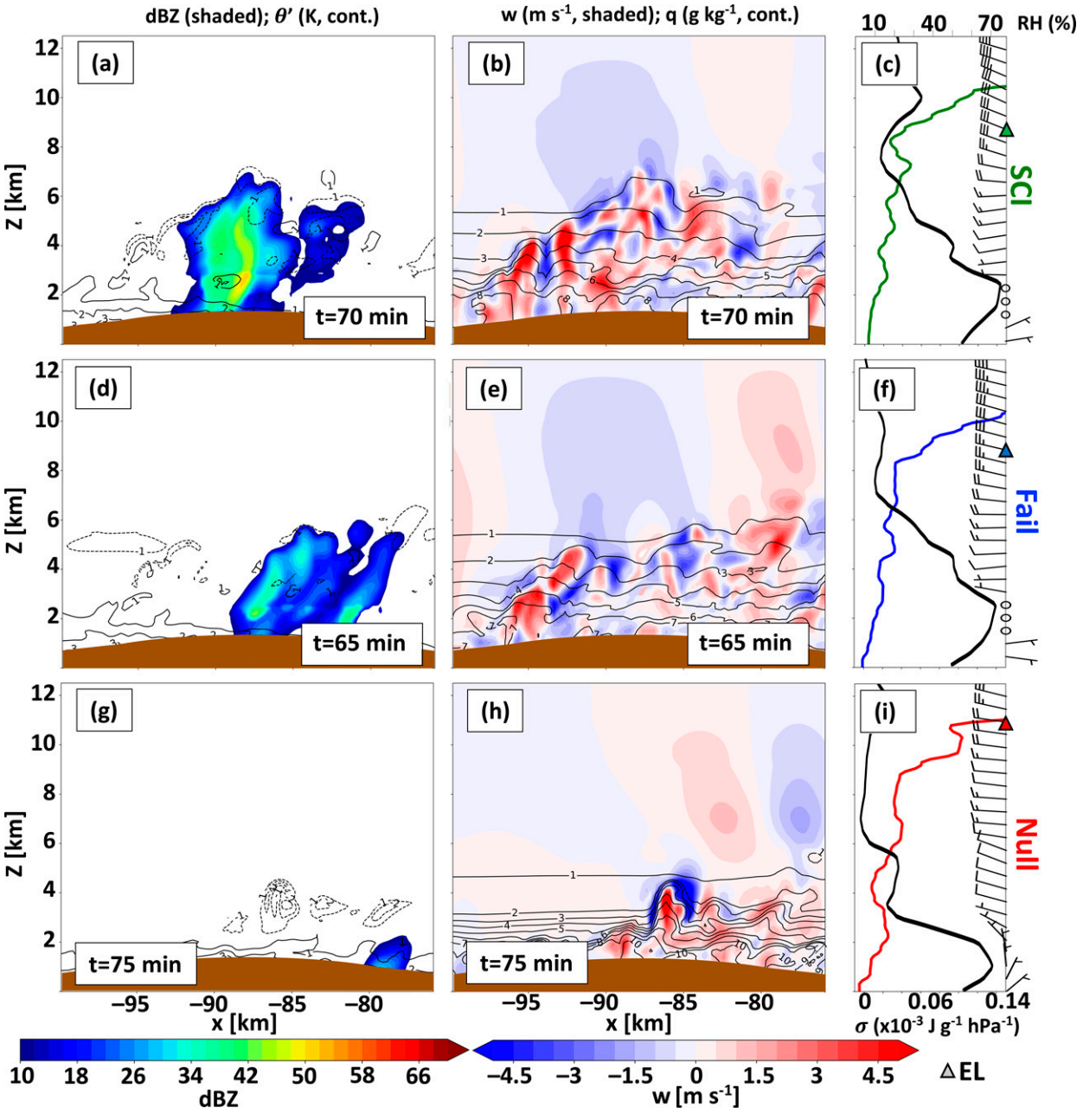

FIG. 5. Cross sections of the (a)–(c) SCI, (d)–(f) Fail, and (g)–(i) Null simulations. All cross sections are E–W across the maximum peak of the terrain (thick black line in Fig. 4). (a),(d),(g) Reflectivity (dBZ, shaded) and potential temperature perturbation from the initial ($t = 0$ h) state (K, contours). The heights of the environmental EL (triangles on the rightmost axis) are representative of a surface-based parcel at the terrain peak 10 min before CI. (b),(e),(h) Vertical velocity (m s^{-1}, shaded) and mixing ratio (g kg^{-1}, contours). (c),(f),(i) Static stability (bottom axis) and RH (top axis) of the initialized sounding. Included in the right-side cross sections in (c), (f), and (i) are the horizontal winds (barbs, right-hand axes).

This increased width and a significantly larger number of tracked updraft thermals yields much larger overall domain-wide vertical mass flux in the NW Null environment (Figs. 6e,f and 7b). However, there is not a comparable difference in thermal width between the base and NW SCI simulations (Fig. 7a). The larger radii and mass flux at $z > 4$ km ATP in the NW Null run compared to the SCI run suggest that these differences are a result of the significantly larger amount of deep CAPE present in the Null thermodynamic environment. Updrafts in both NW SCI and Null simulations contain greater buoyancy at higher altitudes than their base SCI and Null counterparts ($z > 3$ km ATP; Figs. 8e,f). Cloudy updrafts

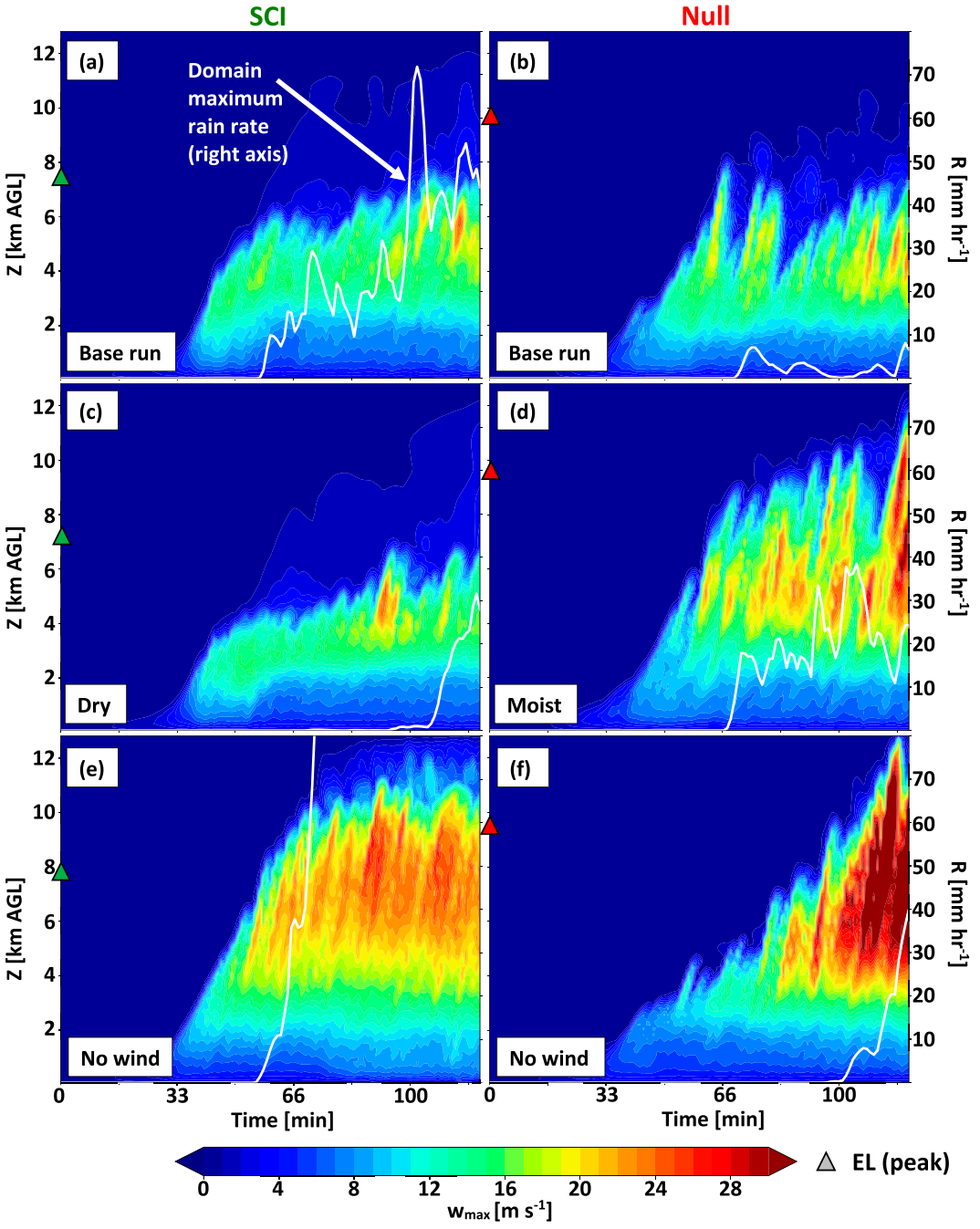

FIG. 6. Hovmöller diagrams of domainwide maximum vertical velocity (m s^{-1}, shaded) as a function of time (bottom axis) and altitude (left axis) and rain rate as a function of time (mm h^{-1}, white line, right axis) for the (a),(b) base SCI and Null, (c),(d) dry SCI/moist Null, and (e),(f) SCI and Null with no wind simulations including terrain, radiation, and surface fluxes. The ELs, denoted with triangles on the left-hand axes, are representative of a surface-based parcel at the top of the terrain 10 min before CI.

from both the NW SCI and NW Null simulations preserve a far greater concentration of boundary layer air per height than those from their windy base environment counterparts at $z > 4$ km ATP (cf. Figs. 10a,b,e,f and 11a). This suggests that entrainment and buoyancy dilution rates are reduced in a calm environment. However, NW Null thermals still appear to suffer greater dilution and cloud water evaporation rate (Figs. 10e,f and 11a) over their full depths than NW SCI thermals, similar to the base simulations, because of the drier free troposphere in the Null profile.

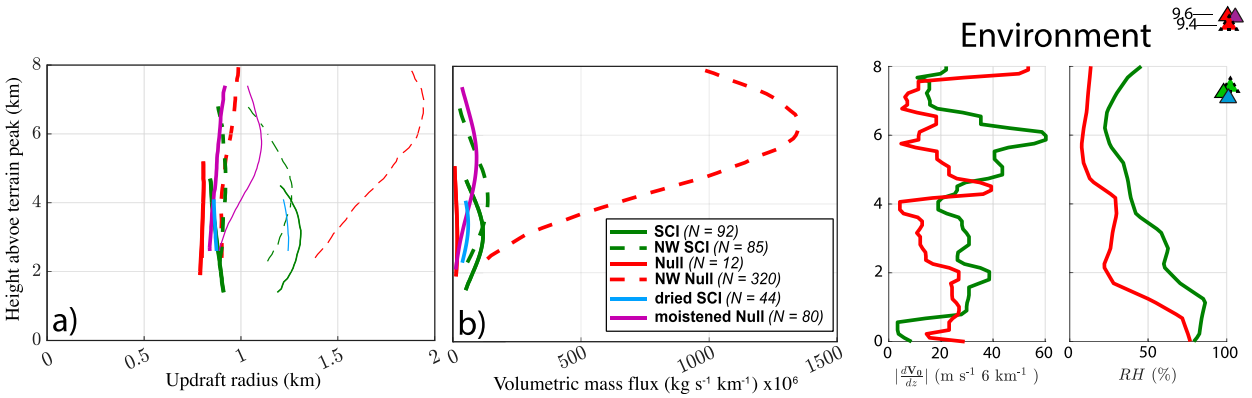

FIG. 7. Tracked thermal characteristics for the base SCI (green, solid), base Null (red, solid), SCI NW (green, dashed), Null NW (red, dashed), dry CI (blue, solid), and moist Null (purple, solid) runs including (a) the mean (thick) and 90th-percentile (thin) thermal radii and (b) the volumetric mass flux. Environmental profiles of wind shear and relative humidity are shown on the right. The EL representative of surface-based parcels from the peak of the terrain are shown by triangles on the right axis. The ELs for the Null simulations are off-axis but are shown to the top right of the plot.

OTHER WIND PROFILE SENSITIVITY SIMULATIONS

To further determine if differences in CI outcome are sensitive to each base wind profile, we performed an additional simulation utilizing an environment composed of the base Null thermodynamic and moisture profile, but prescribed the base SCI wind profile. Isolated and transient precipitating cells initiate late in the simulation (t = 105 min), delayed approximately 45 min from initiation in the base Null run and approximately 10 min from the NW Null run (Figs. 13a,b,d). Maximum updraft height is significantly suppressed in this scenario (Figs. 13a,b and 14a,b) partly from recharacterization of the low-level winds to include stronger cross-terrain flow such that the accumulation of buoyancy near the ridgeline is disrupted (e.g., Hagen et al. 2011; Kirshbaum 2011, 2013).

A final sensitivity experiment isolated the shear effect occurring within the free troposphere from mechanically induced ascent along the terrain associated with the low-level background wind. This was done by setting the wind speed in the base Null environment profile to zero at $z < 4$ km MSL (called the "cropped" wind Null run); thereby, allowing the natural thermally induced orographic circulation in the boundary layer to evolve unmodified by low-level upslope flow. Due to the increased vertical wind shear at z = 4 km MSL, gravity waves develop near the area of the relatively strong static stability in this simulation. Because these waves occur along the shear zone and have a relatively small 2–5 km wavelength, they may be shear–gravity waves (i.e., Kelvin–Helmholtz billows); however, they originate downstream of the terrain within a stable layer, like leeside internal gravity waves, and are also relatively long lived and eventually move upward like vertically propagating waves. A thorough diagnosis of their classification is beyond the scope of this study; therefore, we refer to them more generally as gravity waves. The wave activity has updrafts with magnitudes as strong as ~6 m s^{-1} between z = 4–6 km MSL and t = 25–75 min that precede the thermals erupting from the boundary layer (Fig. 13c).

Generally, the behavior of the convective updrafts in the cropped Null experiment lies between that of the base and NW Null experiments (Figs. 9b,d,e, 13a,c,d, and 14a,c,d). Ascending boundary layer thermals are suppressed early in the simulation (t = 30–80 min) compared to the base Null simulation, but reach a greater altitude and magnitude after 80 min. However, updrafts generally are not as deep or as strong as those in the NW Null simulation. At $z > 4$ km, the concentration of boundary layer air is greater within the cropped Null updrafts than the base Null updrafts but less than at similar altitudes in the Null NW updrafts (Figs. 14a,c,d), implying an intermediate amount of net entrainment of free-tropospheric air into the cloud column in the cropped Null updrafts. These varied entrainment amounts imply proportionally varied dilution of updraft buoyancy based on the similar relative humidity profiles among the Null, cropped Null, and NW Null experiments (e.g., negative regions in Fig. 15). This may be partly evidenced by the Null full wind simulations (base and SCI wind) exhibiting stronger cloud evaporation rates during the updraft growth period compared to the cropped or NW Null simulation (cf. t = 33–60 min in Fig. 14a, t = 33–90 min in Fig. 14c,d). However, both the cropped and NW Null simulations produce similar cloud evaporation rates and in-cloud buoyancy over analogous updraft depths (Figs. 14c,d and 15c,d). Yet updrafts in the cropped Null simulation are generally weaker near the time of CI (cf. Figs. 14c,d at $z > 3$ km and $t > 90$ min). With all other environmental characteristics similar, this suggests that the wind profile in the free troposphere reduces updraft strength in the cropped Null compared to the NW Null simulation, possibly by way of opposing VPGAs (e.g., Peters et al. 2019). Indeed, mean opposing VPGAs between z = 3–6 km are weaker for NW Null updrafts than for the base Null and cropped Null updrafts (Figs. 9 and 11b). Furthermore, opposing VPGAs are the strongest relative to buoyancy at all heights in the updrafts from the simulation using Null thermodynamics but a SCI wind profile, which contains the greatest wind shear (Fig. 11b).

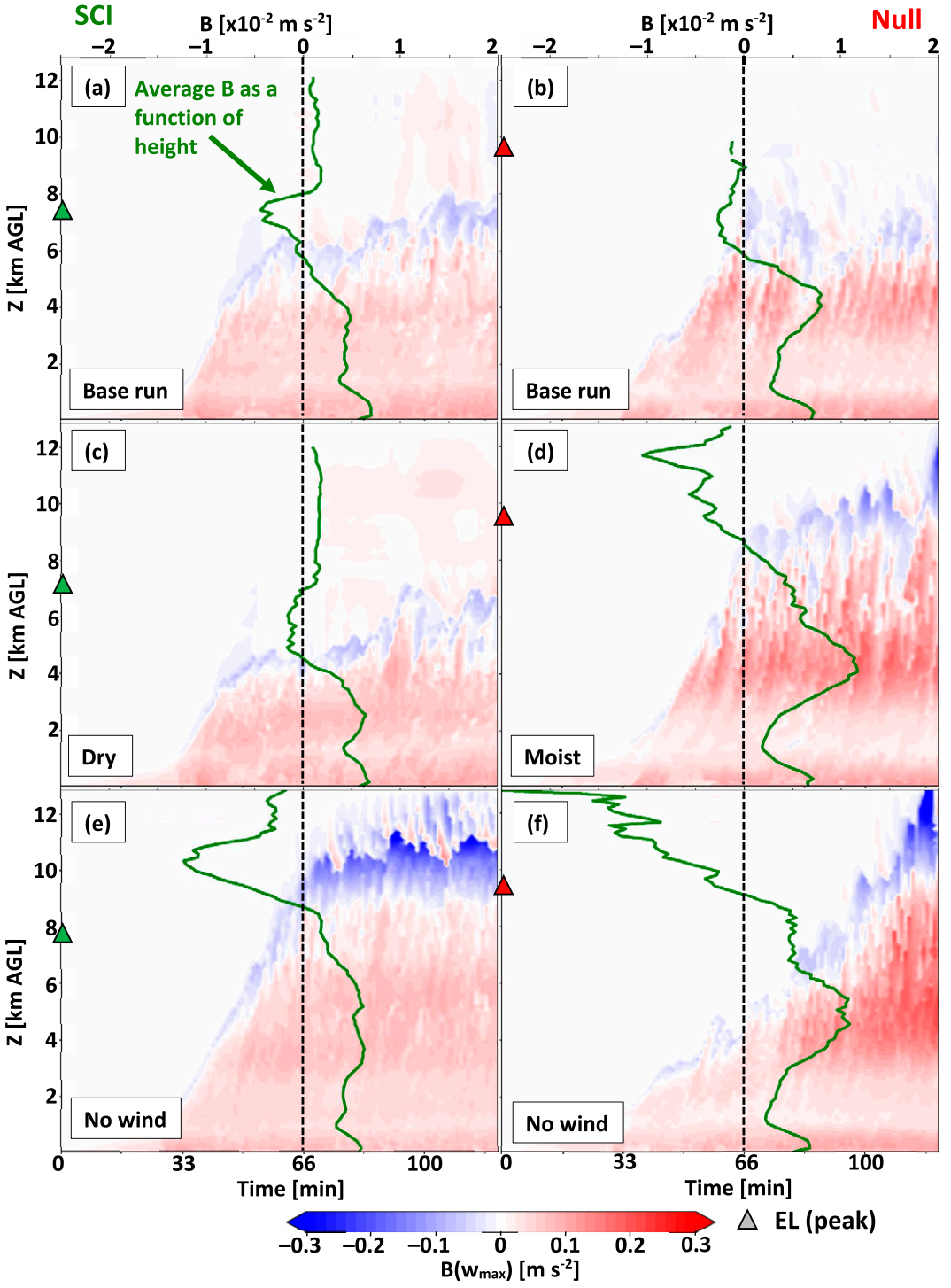

FIG. 8. As in Fig. 6, but for buoyancy (B, m s^{-2}, shaded) at the locations of domainwide maximum velocity shown in Fig. 6 and mean vertical profile of B within updrafts (green line, top axis).

Differences in the characteristics of individual ascending thermals in the NW Null and cropped Null runs may also be sensitive to the details of their encounter with updraft or downdraft branches of the gravity waves. As may be expected, ascent of thermals is generally suppressed upon encountering downdrafts and enhanced upon encountering updrafts associated with the gravity waves. As an upward branch of the wave interacts with the boundary layer thermals comprising the orographic updraft region in the cropped Null simulation, net vertical velocity and depth of the mesoscale

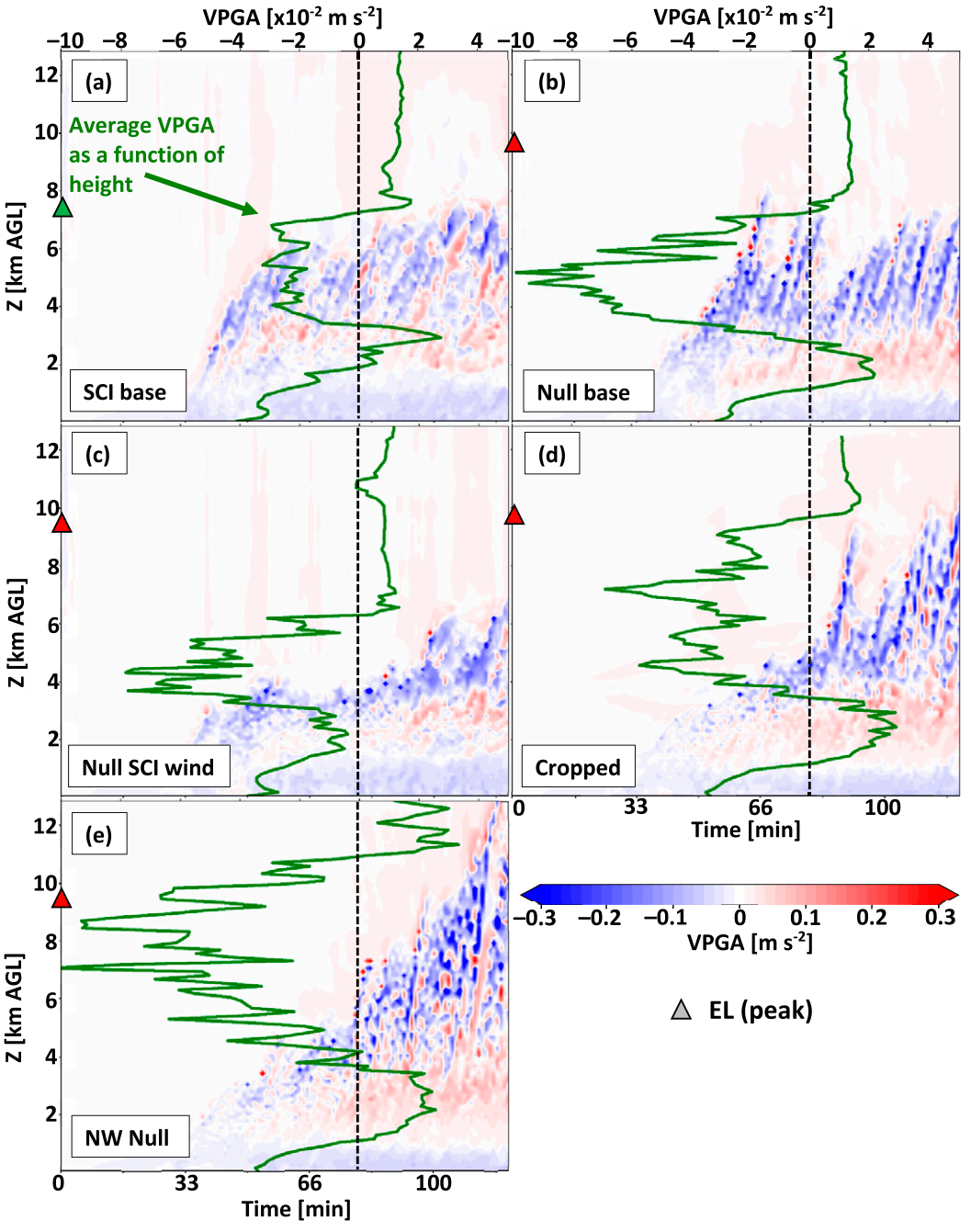

FIG. 9. Hovmöller diagrams of VPGA (m s^{-2}, shaded) as a function of time (bottom axis) and altitude (left- axis) at the locations of domainwide maximum velocity shown in Fig. 6 for the (a) base SCI, (b) base Null, (c) Null with SCI wind, (d) Null with cropped wind below 4 km, and (e) Null with no wind. The mean vertical profile of VPGA within updrafts is shown in green (top axis).

updraft are increased by $O(1)$ m s^{-1} and $O(100)$ m, respectively. Eventually, the orographic updraft deepens through the wave layer and robust precipitating convection occurs from additional rising boundary layer thermals at $t \sim 100$ min (Fig. 13c). Environmental moistening from these thermals interacting with the shear layer may be another reason that updrafts from the cropped run reach higher altitudes and have stronger maximum updraft strengths than the base Null run (~8 vs 6 km AGL; Figs. 13a,c), but ultimately suffer from entrainment-driven dilution and negative VPGAs in the dry free troposphere above this layer (Figs. 9b,d, 11b, and 14a,c). Thus, the simulation of these gravity waves indicates a

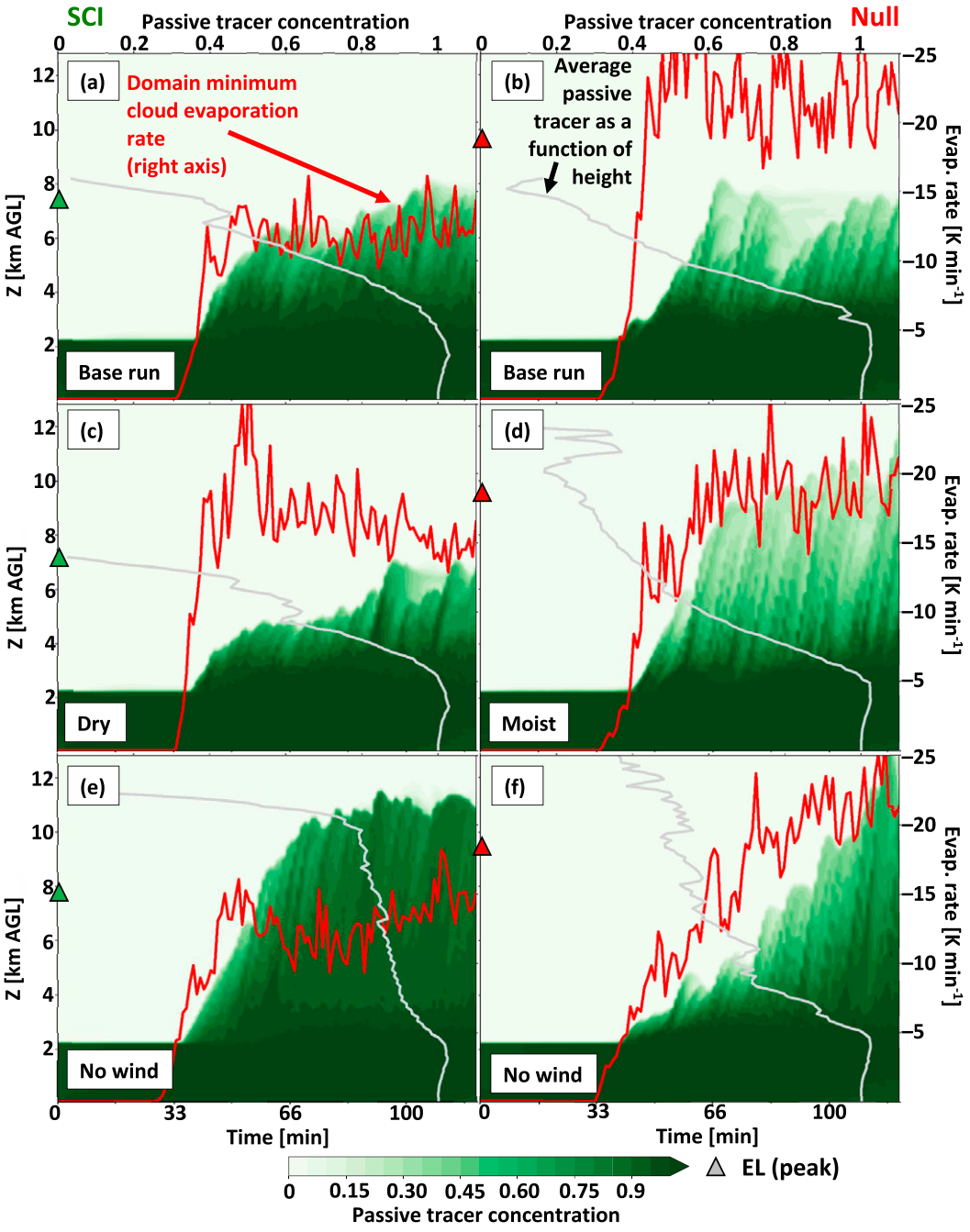

FIG. 10. As in Fig. 6, but for maximum boundary layer passive tracer (shaded), mean passive tracer concentration (white line, top axis), and cloud evaporation rate (K min^{-1}, red line, right axis).

scenario in which ascending thermals may not always be suppressed by strong environmental wind shear.

4. Flat-terrain sensitivity tests

Given the prominent role of the terrain on CI in our simulations shown above, we performed a few additional simulations with no surface fluxes, radiation, or terrain to examine the sensitivity of CI without the presence of orographically induced mesoscale ascent. In these experiments, convective updrafts were initiated by prescribing an individual ellipsoidal temperature perturbation (i.e., "thermal") within the boundary layer at the model initialization time. The thermals had a maximum magnitude of +2 K, and a 1.5-km

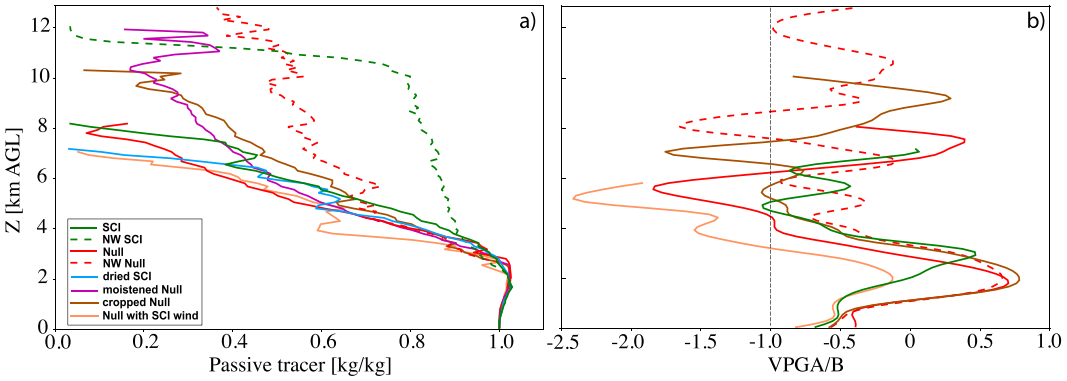

FIG. 11. Vertical profiles of time mean (a) boundary layer passive tracer and (b) ratio of VPGA and buoyancy (VPGA/B) from the following simulations: base SCI (green solid), base Null (red solid), SCI NW (green dashed), Null NW (red dashed), dry CI (blue solid), and moist Null (purple solid). The passive tracer profiles are also shown in Figs. 10 and 14 individually. The vertical dashed line in (b) denotes VPGA/$B = -1$. A ratio of -1 implies that VPGA offsets (i.e., balances) buoyant accelerations, with values < -1 primarily being downward VPGA dominant and values > -1 primarily being B dominant.

vertical and 5-km horizontal diameter centered at 0.75 km AGL.[8] These parameters were chosen based on sensitivity experiments testing a variety of horizontal and vertical thermal diameters (2.5–7.5 km, 1–2 km, respectively) and magnitudes (+1–3 K). Deep convective structure was the most sensitive to the horizontal diameter. A thermal width of 5 km was the narrowest thermal producing precipitating convection in the base SCI environment. Coincidentally, CI also first occurred in the base Null environment with a 5-km-wide prescribed thermal. Thus, the presence of CI across the SCI and Null environments in these flat-terrain simulations was insensitive to the tested prescribed thermal widths. We comment more upon the ramifications of this insensitivity below.

Ascent of the prescribed thermal in the base SCI and Null environments yields a singular precipitating updraft (Fig. 16). The updraft in the flat-terrain SCI simulation ascends to $z \sim 5.5$ km AGL, similar to the height ATP achieved in the terrain-inclusive SCI simulation, but falling short of the EL predicted by lifting a surface parcel from the base-state environment (8.5 km AGL) (cf. Figs. 6a and 16a). Although a slightly stronger precipitating updraft is produced in the Null environment, it reaches a similar height as in the SCI simulation and falls quite short of its surface-based parcel EL (10.8 km AGL) (cf. Figs. 6b and 16b).

To help further isolate shear suppression effects upon ascending thermals from the mesoscale orographic circulation, we set the ambient wind profile equal to zero as in the "NW" experiment shown in section 3c (Figs. 16c,d). As in the terrain-inclusive NW simulations, updrafts in the flat-terrain NW SCI and NW Null simulations are stronger, reach their predicted surface-based Els, and yield generally larger maximum near-surface rainfall (cf. Figs. 6e,f and 16c,d). Further, the flat-terrain NW Null updraft achieves a similarly intense magnitude as its terrain-inclusive counterparts at $t > 90$ min. Thus, convective updraft behavior occurring in the absence of a mesoscale lifting mechanism further confirms the suppressing effects of vertical wind shear on deepening clouds.

It is important to note that a natural evolution of progressively deepening clouds is not necessarily captured in these simulations. For example, the prescribed thermal in the flat-terrain NW Null simulation rises quite rapidly to its EL, while a longer period of consolidation of boundary layer buoyancy along the ridgeline is required to generate sustained updrafts in the terrain-inclusive NW Null simulation (cf. Figs. 6f and 16f). The immediacy of updraft growth in this flat-terrain experiment is related to our prescription of a 5-km-wide boundary layer thermal, which was required to achieve precipitating updrafts in the SCI environment. Thus, it is important to exercise caution when employing a prescribed thermal methodology to initiate deep updrafts in convective simulations, especially given the sensitivity of entrainment and shear effects to updraft width (e.g., Morrison 2017; Lecoanet and Jeevanjee 2019; Morrison et al. 2020; Peters et al. 2019, 2020, 2022a,b).

5. Discussion

Altering the humidity profiles in the free troposphere of the SCI and Null environments had profound effects on entrainment-driven dilution of updrafts. All other parameters left unaltered, a moistened Null free troposphere produced numerous deep updrafts with strong buoyancy and large precipitation rates. Though artificially dried SCI environments still yielded precipitating convection, updrafts were generally less buoyant, shallower, and yielded smaller precipitation rates than the base SCI environment. This supports the hypothesis that entrainment of free-tropospheric dry air alone is a prominent governor of deep CI in the observed RELAMPAGO-CACTI cases, similar to conclusions by other studies using idealized environmental profiles (Crook 1996; Zhao and Austin 2005; Damiani et al. 2006; Houston and Niyogi 2007;

[8] Note that AGL is the same as MSL in these flat-terrain simulations.

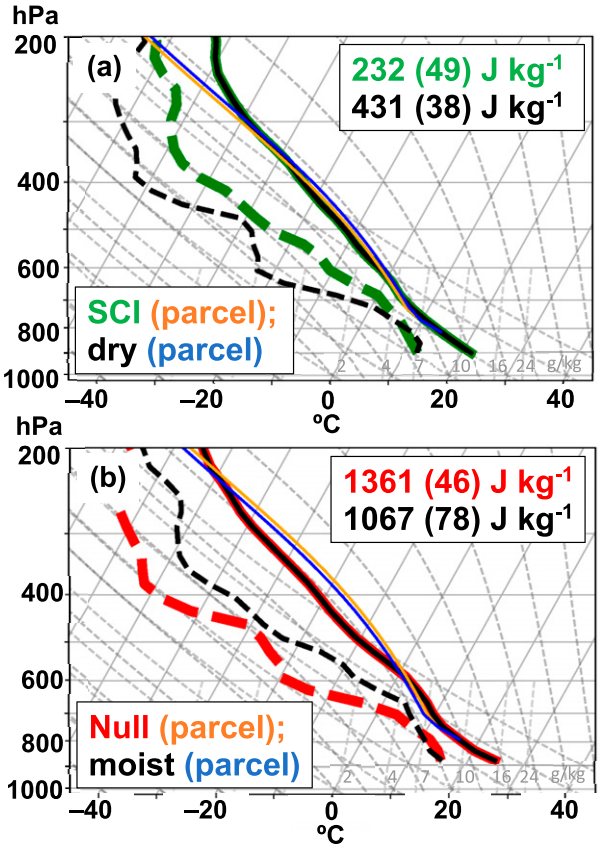

FIG. 12. Modified SCI and Null soundings, where (a) the SCI sounding (green) is dried using the Null dewpoint depression (black), and (b) the Null sounding (red) is moistened using the SCI dewpoint depression (black). Lifted parcels representative of the mean of the lowest 100-hPa-deep layer of the sounding ("ML" parcel) are shown for the base soundings (orange) and the modified soundings (blue). ML CAPE (ML CIN) is provided for each sounding in the top-right corner.

Romps 2010; De Rooy et al. 2013; Hernandez-Deckers and Sherwood 2016, 2018; Morrison 2017; Moser and Lasher-Trapp 2017; Rousseau-Rizzi et al. 2017; Leger et al. 2019; Morrison et al. 2020; Peters et al. 2019, 2020).

Results from our experiments suggest somewhat separable impacts of the wind profile upon the character of ascending updrafts and the probability of CI. While clouds interacting with deep vertical wind shear are suppressed, consistent with the findings of Peters et al. (2019, 2022a,b), Morrison et al. (2020), and Peters et al. (2020), changes in the low-level flow affect mesoscale ascent and accumulation of buoyancy realized along the terrain (Kirshbaum 2011, 2013). Past literature sometimes causally implicates shear in the direct modification of entrainment of clouds and updrafts (Markowski et al. 2006; Wang et al. 2008; Markowski and Richardson 2010; Wang et al. 2012). However, other studies show that there may not be a change in the net entrainment rate near thermals ascending in ambient wind shear; rather, entrainment is increased on the downshear side of clouds and decreased on the upshear side (e.g., Zhao and Austin 2005). It is possible that shear may play indirect roles in dilution of clouds through updraft-suppressing VPGAs that would increase the residence time of individual ascending thermals within the dry free troposphere prior to the production of precipitation. This conclusion may be akin to one made by Markowski et al. (2006), where relatively deep cumulus are fueled by upright subcloud inflow trajectories owing to weak ambient wind shear, along which less dilution via entrainment could occur than if trajectories are significantly tilted by stronger shear prior to reaching their LFC. Collectively, this suggests that the relatively shallow cloud-top heights in the base SCI and Null runs are due to a culmination of factors, including adverse VPGAs, terrain–flow interactions and the disruption of mesoscale convergence of low-level buoyancy, and subsequent dilution of buoyancy by entrainment.

Some recent studies highlight preconditioning of the environment through detrainment of cloudy air from predecessor updrafts within thermal chains as being an important part of the CI process (Damiani et al. 2006; Kirshbaum 2011; Varble et al. 2014; Hernandez-Deckers and Sherwood 2016; Moser and Lasher-Trapp 2017). Our results indicated some circumstantial evidence that this may have encouraged CI in many of our terrain-inclusive calm wind simulations because the earliest updrafts often were shallower than subsequent ones (Figs. 6a,b,e,f). However, it is not clear if this effect is a necessary condition for CI because the presence of background wind shear in the base SCI runs yielded a cloud-relative and terrain-relative mean wind that may advect moisture away from the geographical region where clouds are deepening. A detailed analysis of the importance of this effect in the context of our numerical experiments is planned as future work.

The greatest sensitivity in thermal width across our experiments was realized by the largest thermals in each simulation, and the overall widest updrafts occurred in the environments with the most significant orographic circulations, consistent with Hernandez-Deckers and Sherwood (2016) and Rousseau-Rizzi et al. (2017). Updraft radius varied by < 0.2 km across our terrain-inclusive SCI experiments. However, the widest updrafts in the NW Null and moistened Null experiment were significantly larger than in the base Null environment, by as much as 0.4 or 2.0 km in diameter (moistened and NW, respectively) over the base Null environment. Based on this sensitivity and comparisons to flat-terrain experiments (sections 3 and 4, respectively), we conclude that the orographic mesoscale updraft appeared to play a key role in allowing thermals that spatially scale with the depth of the boundary layer (~1–2-km diameter) to achieve CI. It was necessary to prescribe much wider thermals in the flat-terrain simulations, which lacked a mesoscale forcing mechanism, in order to achieve CI. Observed thermal sizes may not be the same across the three observed event types owing to complex mesoscale environments. For example, thermals associated with Fail or Null events may be smaller and/or weaker than in SCI events, making them less able to withstand buoyancy dilution by entrainment. This is perhaps consistent with our measurements of updraft width across our base SCI and Null simulations (90th percentile radii measurements in Fig. 7a), and may be consistent

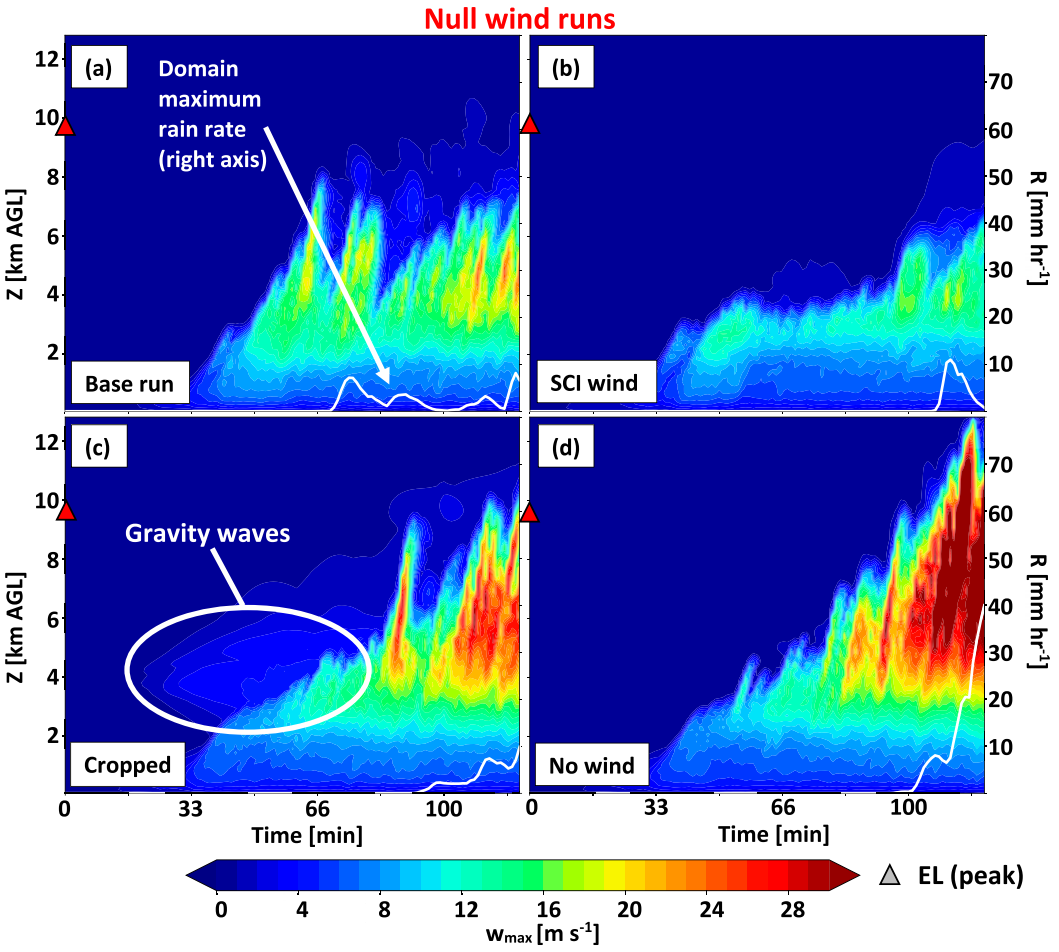

FIG. 13. As in Fig. 6, but for (a) the base Null run, (b) Null with SCI wind, (c) Null with cropped wind below 4 km, and (d) Null with no wind.

with dual-Doppler observations of low-level updraft size across differing CI outcomes (Marquis et al. 2021).

Finally, Nelson et al. (2021) indicate that parcel CAPE is statistically larger and environmental freezing level is statistically higher for Null events than for SCI events. We did not directly modify CAPE, freezing level, or other static stability layer properties in our experiments owing to the complexity of altering them in isolation of other environmental factors affecting CI. Instead, we focused on modifications identified by Nelson et al. (2021) that could affect the CI outcome but are not necessarily directly considered by traditional parcel theory. Tian et al. (2021) exchange the temperature profiles of shallow and deep cumulus environments evaluated with a plume entrainment model. They find a larger sensitivity of the growth of cumulus to the low-level temperature profile (by way of altered instability and the related ease for a parcel to reach its LFC) than to the upper level temperature profile. Instead the growth of cumulus was more sensitive to environmental moisture in the upper free troposphere. Though we do not alter the temperature profiles directly, our suite of experiments exchanging moisture and wind profiles among SCI and Null conditions offers de facto inferences about the exchange of stability profiles. The base SCI environment has less full-tropospheric CAPE, more CIN, weaker low-level (i.e., 800–600 hPa) integrated buoyancy, and a higher LFC than the base Null environment, yet more prolific convection occurs in SCI simulations in their seemingly inferior low-level environment. Further, deeper convection occurs in the moistened Null environment, which ironically, has smaller full-tropospheric CAPE, larger CIN, and a higher LFC than the base Null environment. Thus, CI in our simulations exhibits a lower sensitivity to low-level instability than in Tian et al. (2021), but appears to bear sensitivities to upper-level moisture and insensitivity to upper-level stability similar to theirs. We hypothesize that the relative insensitivity to low-level stability in our simulations results from the presence of the mesoscale lift associated with our orographic circulations.

6. Summary

We conducted a series of high-resolution simulations employing horizontally homogeneous base states composed of

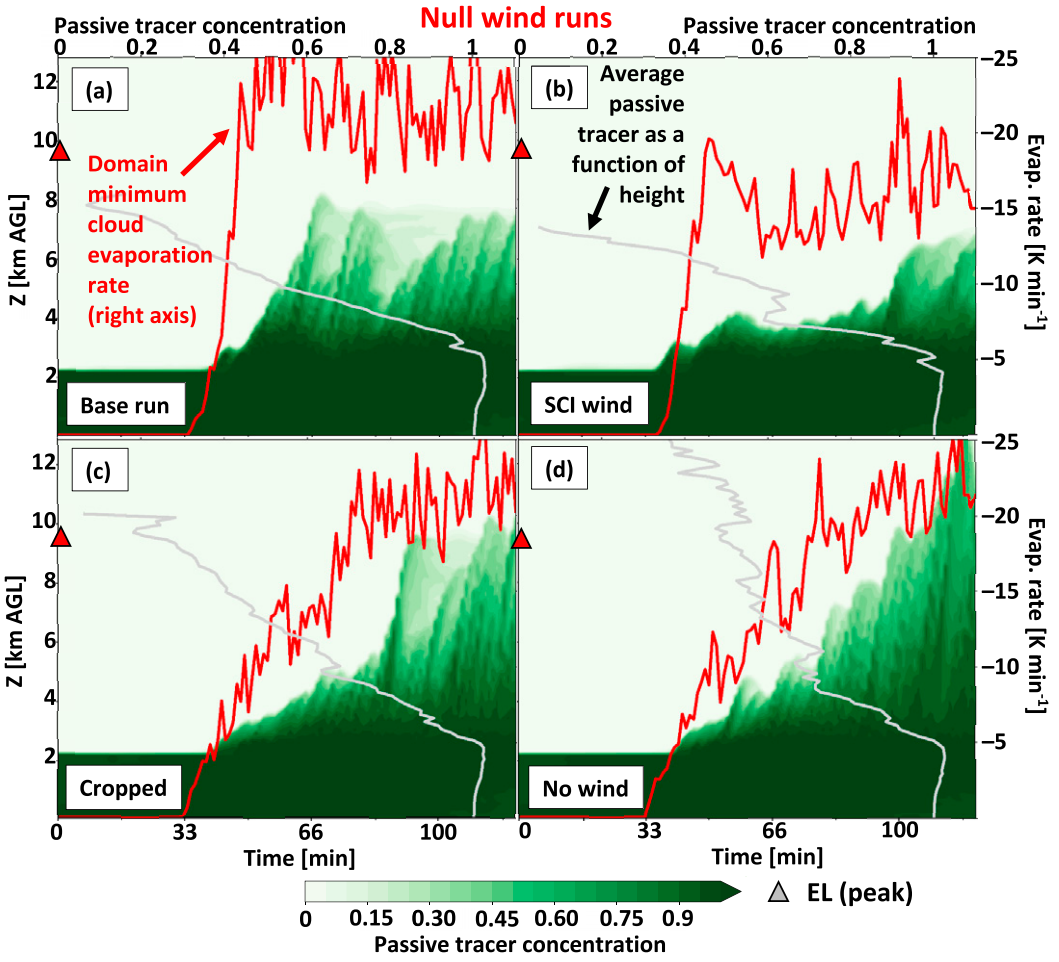

FIG. 14. As in Fig. 13, but for maximum boundary layer passive tracer (shaded), mean passive tracer concentration (white line, top axis), and cloud evaporation rate (K min^{-1}, red line, right axis).

radiosonde profiles supporting a variety of deep CI outcomes observed along the Sierras de Córdoba range in central Argentina during the RELAMPAGO and CACTI field campaigns. Our goal was to relate specific convective updraft processes associated with successful and unsuccessful CI outcomes to the surrounding environmental shear, moisture, and orographically induced mesoscale flow. We evaluated convective updraft width, depth, strength, and processes modulating them, such as thermal buoyancy, inferred entrainment and dilution rates, and opposing vertical pressure gradient accelerations across 13 simulations that utilize composite observed environments and variations upon them as initial conditions. Experiments comparing the simulations supported the following conclusions:

1) Thermally induced orographic ascent aided the ascent of 1–2-km-wide boundary layer buoyant thermals to their LFCs during the CI process. Without this focused mesoscale convergence and ascent, much wider (~5-km-diameter) boundary layer thermals were required to yield CI.
2) Altering the humidity profiles in the free troposphere of the SCI and Null environments had a profound influence on CI. The entrainment of free-tropospheric dry air was a salient factor governing maximum updraft depth and buoyancy in the RELAMPAGO-CACTI environments.
3) Though the maximum achievable depth of convection was quite sensitive to the free-tropospheric shear, the ability for boundary layer thermals to reach their LFC was highly sensitive to the low-level winds that alter the character of orographic mesoscale ascent.
4) Mean updraft radius was not significantly different across our terrain experiments. Though differences in updraft width were small in experiments using the SCI thermodynamic environment, the largest simulated updrafts in the Null thermodynamic environments were ~0.4–2.0 km wider in the most humid and calm conditions. Thus, thermal width is perhaps most consistently sensitive in conditions with large static instability.

Collectively, our findings confirm that both wind and moisture profiles are key factors in the CI process. Specifically, the

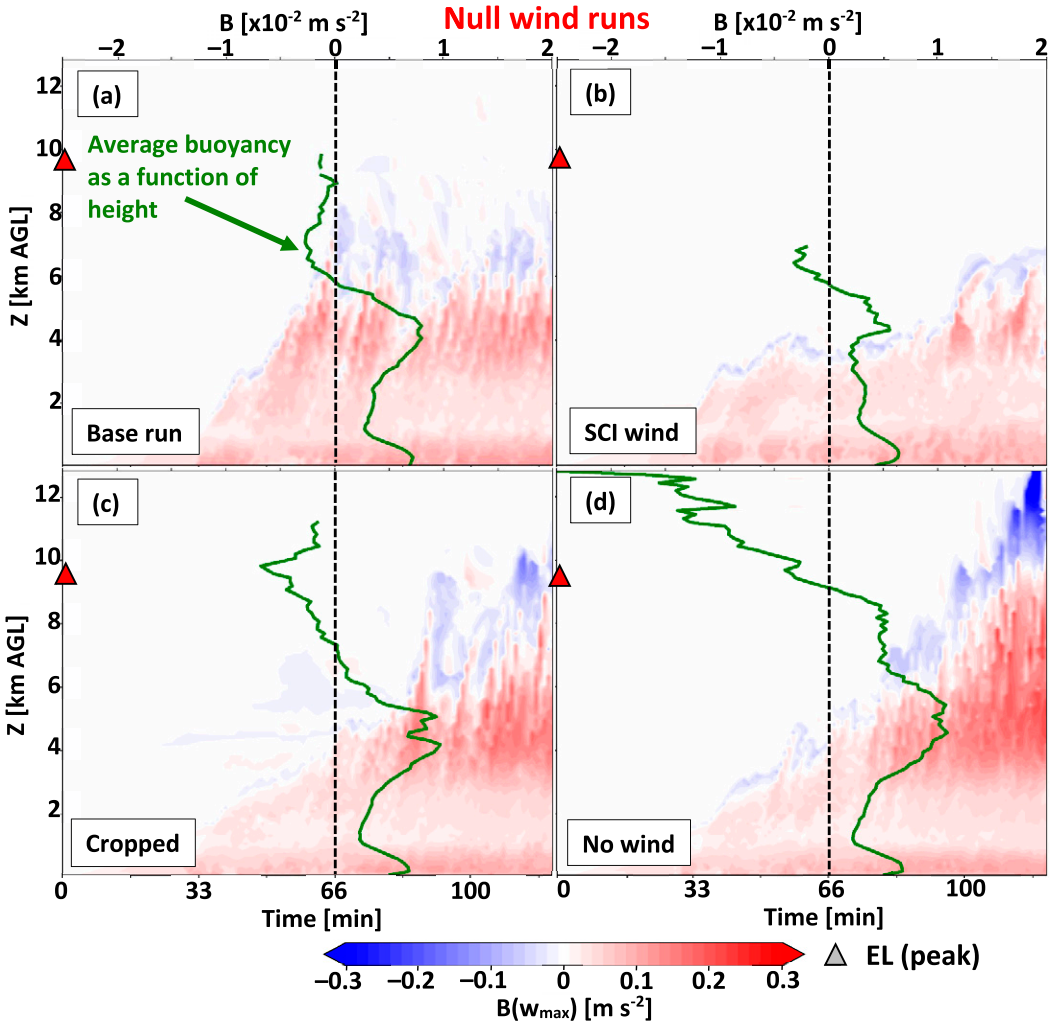

FIG. 15. As in Fig. 13, but of buoyancy (B, m s^{-2}, shaded) at the locations of domainwide maximum velocity shown in Fig. 13 and mean vertical profile of B within updrafts (green line, top axis).

combined effects of adverse VPGAs (via vertical wind shear), terrain–flow interactions (via upslope flow and organized mountain top convergence), and strength of thermal buoyancy dilution (via dry air entrainment), dictated the probability of CI. However, it was not always possible to clearly disentangle the effects of shear from moisture variation on thermal width and buoyancy, opposing pressure gradient forces, and entrainment processes because many of these processes feedback on each other. For example, if the primary suppressing effect of shear is to yield downward-oriented VPGAs that oppose ascending thermals, this would be expected to increase the exposure period of clouds to entrainment of dry free-tropospheric air before they can effectively generate precipitation. A more complete disentanglement of the relative roles of boundary layer and free-tropospheric shear on updrafts was complicated by the introduction of gravity waves.

It was our primary goal to better understand how cumulus updrafts interact with the ambient near-cloud environment under somewhat simplified and controlled conditions (e.g., initial environmental horizontal homogeneity and omission of the background synoptic conditions). Our experimental design provided some clues to the relative roles of the ambient wind interacting directly with the cloud and also with the terrain to affect the local mesoscale orographic circulation. However, it is important to acknowledge that our relatively idealized model design likely underrepresents fully realistic orographically induced convergence originating from its interaction with complex heterogeneous flow, such as leeside flow convergence regions often observed and simulated in mountain convection scenarios. Future cloud-scale simulations should consider these complicated conditions in relation to updraft interactions with the near-cloud environment.

Domain mean volume mass flux increased in our simulations in which calm winds are prescribed (compared to those with the composite environmental wind profiles prescribed) owing to increased orographic convergence and less disruption of buoyancy accumulation near the terrain. Wind shear would also be expected to increase the cloud-relative wind

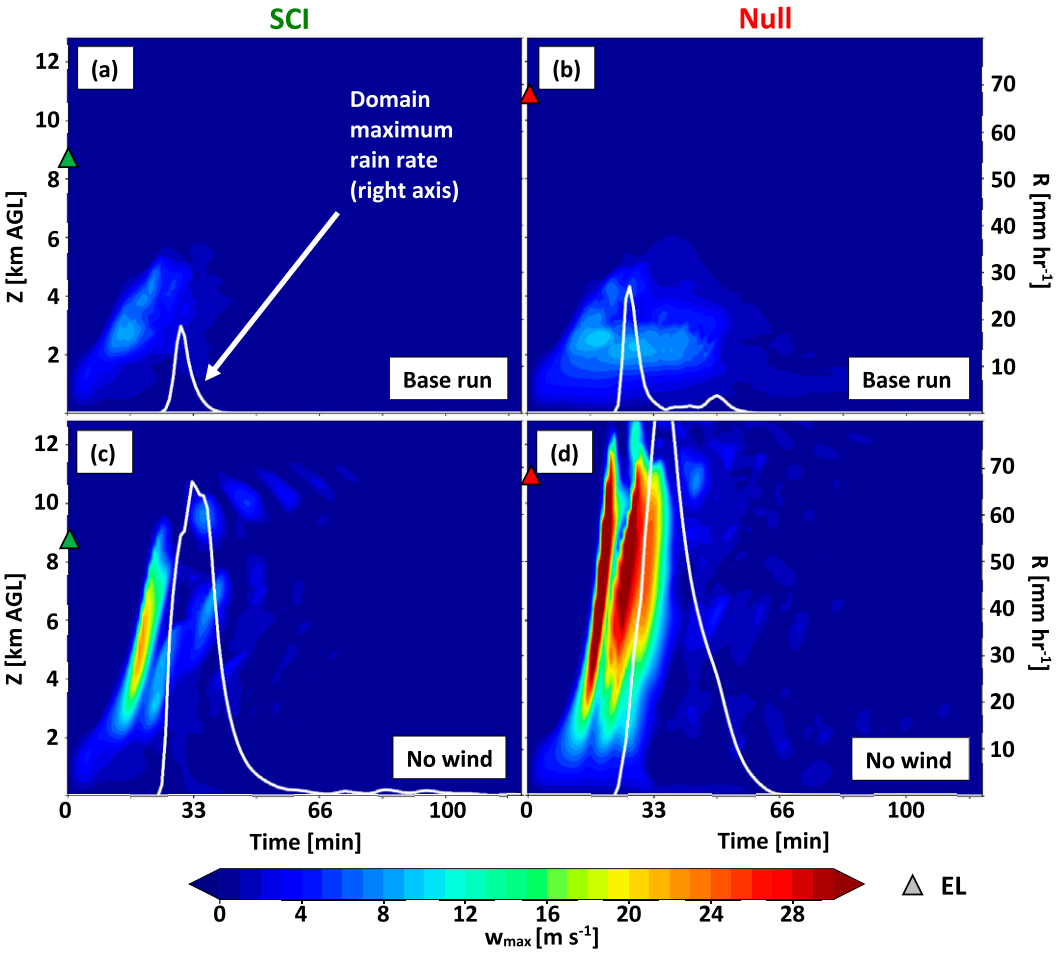

FIG. 16. As in Fig. 6, but for the base (a),(c) SCI and (b),(d) Null simulations releasing a prescribed thermal with no terrain or surface heat fluxes (a),(b) with and (c),(d) without wind. Environmental EL are representative for a surface-based parcel at $t = 0$ min.

field, which may also increase the vertical mass flux per individual updraft. Contemporaneous work by the authors further examines this concept in detail (e.g., Peters et al. 2022a,b). Finally, given the importance of updraft width on the ultimate CI outcome, it is important to better understand the initial controls of updraft width at low levels. In particular, future work should focus on understanding the environmental factors controlling the width of boundary layer thermals as they transition through the boundary layer cap and into the free troposphere, particularly in the context of realistic mesoscale forcing mechanisms like the thermally induced orographic circulation examined in this study.

Acknowledgments. T. Connor Nelson's, James N. Marquis's, and Katja Friedrich's work was supported by NSF Grant AGS-1661707 and by the U.S. Department of Energy's of Science Biological and Environmental Research as part of the Atmospheric System Research program. John Peters's work was supported by NSF Grants AGS-1928666, AGS-1841674 and DOE-ASR Grant DE-SC0000246356. Pacific Northwest National Laboratory is operated by Battelle for the U.S. Department of Energy under Contract DE-AC05-76RLO1830. Simulations were performed using George Bryan's CM1 model on NCAR's Cheyenne supercomputing facility. Thank you to CISL for supporting these computing activities. We also are thankful for helpful discussions with Adam Varble, Jake Mulholland, Zhe Feng, George Bryan, Nicholas Luchetti, Steve Nesbitt, Itinderjot Singh, Hugh Morrison, and to participants of the RELAMPAGO and CACTI field project for your dedication to collecting the radiosonde data used in this study. We would also like to thank three anonymous reviewers for their input on this work.

Data availability statement. Composite soundings used to initialize the idealized models are discussed by Nelson et al. (2021) and stored on the CU Scholar repository under the title: "Statistical comparisons between convective environments during the 2018/19 RELAMPAGO-CACTI field campaign." Numerical simulation input, output, and code, are stored on NCAR's Computational and Information Systems Lab campaign storage and are available upon request.

REFERENCES

Banta, R., 1984: Daytime boundary-layer evolution over mountainous terrain. Part I: Observations of the dry circulations. *Mon. Wea. Rev.*, **112**, 340–356, https://doi.org/10.1175/1520-0493(1984)112<0340:DBLEOM>2.0.CO;2.

——, and C. B. Schaaf, 1987: Thunderstorm genesis zones in the Colorado Rocky Mountains as determined by traceback of geosynchronous satellite images. *Mon. Wea. Rev.*, **115**, 463–476, https://doi.org/10.1175/1520-0493(1987)115<0463:TGZITC>2.0.CO;2.

Behrendt, A., and Coauthors, 2011: Observation of convection initiation processes with a suite of state-of-the-art research instruments during COPS IOP 8b. *Quart. J. Roy. Meteor. Soc.*, **137** (Suppl. 1), 81–100, https://doi.org/10.1002/qj.758.

Bryan, G. H., and M. J. Fritsch, 2002: A benchmark simulation for moist nonhydrostatic numerical models. *Mon. Wea. Rev.*, **130**, 2917–2928, https://doi.org/10.1175/1520-0493(2002)130<2917:ABSFMN>2.0.CO;2.

——, J. C. Wyngaard, and J. M. Fritsch, 2003: Resolution requirements for the simulation of deep moist convection. *Mon. Wea. Rev.*, **131**, 2394–2416, https://doi.org/10.1175/1520-0493(2003)131<2394:RRFTSO>2.0.CO;2.

Coffer, B. E., and M. D. Parker, 2017: Simulated supercells in nontornadic and tornadic VORTEX2 environments. *Mon. Wea. Rev.*, **145**, 149–180, https://doi.org/10.1175/MWR-D-16-0226.1.

Crook, N. A., 1996: Sensitivity of moist convection forced by boundary layer processes to low-level thermodynamic fields. *Mon. Wea. Rev.*, **124**, 1767–1785, https://doi.org/10.1175/1520-0493(1996)124<1767:SOMCFB>2.0.CO;2.

Damiani, R., G. Vali, and S. Haimov, 2006: The structure of thermals in cumulus from airborne dual-Doppler radar observations. *J. Atmos. Sci.*, **63**, 1432–1450, https://doi.org/10.1175/JAS3701.1.

Davis, C. A., K. W. Manning, R. E. Carbone, S. B. Trier, and J. D. Tuttle, 2003: Coherence of warm-season continental rainfall in numerical weather prediction models. *Mon. Wea. Rev.*, **131**, 2667–2679, https://doi.org/10.1175/1520-0493(2003)131<2667:COWCRI>2.0.CO;2.

Demko, J. C., and B. Geerts, 2010: A numerical study of the evolving convective boundary layer and orographic circulation around the Santa Catalina Mountains in Arizona. Part I: Circulation without deep convection. *Mon. Wea. Rev.*, **138**, 1902–1922, https://doi.org/10.1175/2009MWR3098.1.

De Rooy, W. C., and Coauthors, 2013: Entrainment and detrainment in cumulus convection: An overview. *Quart. J. Roy. Meteor. Soc.*, **139**, 1–19, https://doi.org/10.1002/qj.1959.

Dörnbrack, A., J. D. Doyle, T. P. Lane, R. D. Sharman, and P. K. Smolarkiewicz, 2005: On physical reliability and uncertainty of numerical solutions. *Atmos. Sci. Lett.*, **6**, 118–122, https://doi.org/10.1002/asl.100.

Duda, J. D., and W. A. Gallus, 2013: The impact of large-scale forcing on skill of simulated convective initiation and upscale evolution with convection-allowing grid spacings in the WRF. *Wea. Forecasting*, **28**, 994–1018, https://doi.org/10.1175/WAF-D-13-00005.1.

French, J., G. Vali, and R. D. Kelly, 1999: Evolution of small cumulus clouds in Florida: Observations of pulsating growth. *Atmos. Res.*, **52**, 143–165, https://doi.org/10.1016/S0169-8095(99)00024-1.

Grell, G. A., J. Dudhia, and D. R. Stauffer, 1994: A description of the fifth-generation Penn State/NCAR Mesoscale Model (MM5). NCAR Tech. Note NCAR/TN-398+STR, 121 pp., https://doi.org/10.5065/D62V2D1B.

Hagen, M., J. Baelen, and E. Richard, 2011: Influence of the wind profile on the initiation of convection in mountainous terrain. *Quart. J. Roy. Meteor. Soc.*, **137** (Suppl. 1), 224–235, https://doi.org/10.1002/qj.784.

Hernandez-Deckers, D., and S. C. Sherwood, 2016: A numerical investigation of cumulus thermals. *J. Atmos. Sci.*, **73**, 4117–4136, https://doi.org/10.1175/JAS-D-15-0385.1.

——, and ——, 2018: On the role of entrainment in the fate of cumulus thermals. *J. Atmos. Sci.*, **75**, 3911–3924, https://doi.org/10.1175/JAS-D-18-0077.1.

Houston, A. L., and D. Niyogi, 2007: The sensitivity of convective initiation to the lapse rate of the active cloud-bearing layer. *Mon. Wea. Rev.*, **135**, 3013–3032, https://doi.org/10.1175/MWR3449.1.

Iacono, M. J., J. S. Delamere, E. J. Mlawer, M. W. Shephard, S. A. Clough, and W. D. Collins, 2008: Radiative forcing by long-lived greenhouse gases: Calculations with the AER radiative transfer models. *J. Geophys. Res.*, **113**, D13103, https://doi.org/10.1029/2008JD009944.

Kirshbaum, D. J., 2011: Cloud-resolving simulations of deep convection over a heated mountain. *J. Atmos. Sci.*, **68**, 361–378, https://doi.org/10.1175/2010JAS3642.1.

——, 2013: On thermally forced circulations over heated terrain. *J. Atmos. Sci.*, **70**, 1690–1709, https://doi.org/10.1175/JAS-D-12-0199.1.

——, 2017: On upstream blocking over heated mountain ridges. *Quart. J. Roy. Meteor. Soc.*, **143**, 53–68, https://doi.org/10.1002/qj.2945.

——, 2020: Numerical simulations of orographic convection across multiple gray zones. *J. Atmos. Sci.*, **77**, 3301–3320, https://doi.org/10.1175/JAS-D-20-0035.1.

——, and D. R. Durran, 2004: Factors governing cellular convection in orographic precipitation. *J. Atmos. Sci.*, **61**, 682–698, https://doi.org/10.1175/1520-0469(2004)061<0682:FGCCIO>2.0.CO;2.

——, and C. C. Wang, 2014: Boundary layer updrafts driven by airflow over heated terrain. *J. Atmos. Sci.*, **71**, 1425–1442, https://doi.org/10.1175/JAS-D-13-0287.1.

——, B. Adler, N. Kalthoff, C. Barthlott, and S. Serafin, 2018: Moist orographic convection: Physical mechanisms and links to surface-exchange processes. *Atmosphere*, **9**, 80, https://doi.org/10.3390/atmos9030080.

Lebo, Z. J., and H. Morrison, 2015: Effects of horizontal and vertical grid spacing on mixing in simulated squall lines and implications for convective strength and structure. *Mon. Wea. Rev.*, **143**, 4355–4375, https://doi.org/10.1175/MWR-D-15-0154.1.

Lecoanet, D., and N. Jeevanjee, 2019: Entrainment in resolved, dry thermals. *J. Atmos. Sci.*, **76**, 3785–3801, https://doi.org/10.1175/JAS-D-18-0320.1.

Leger, J., J. P. Lafore, J. M. Piriou, and J. F. Guérémy, 2019: A simple model of convective drafts accounting for the perturbation pressure term. *J. Atmos. Sci.*, **76**, 3129–3149, https://doi.org/10.1175/JAS-D-18-0281.1.

Markowski, P., and Y. Richardson, 2010: *Mesoscale Meteorology in Midlatitudes*. Wiley-Blackwell, 407 pp.

——, C. Hannon, and E. Rasmussen, 2006: Observations of convection initiation "failure" from the 12 June 2002 IHOP deployment. *Mon. Wea. Rev.*, **134**, 375–405, https://doi.org/10.1175/MWR3059.1.

Marquis, J. N., A. C. Varble, P. Robinson, T. C. Nelson, and K. Friedrich, 2021: Low-level mesoscale and cloud-scale interactions promoting deep convection initiation. *Mon. Wea. Rev.*, **149**, 2473–2495, https://doi.org/10.1175/MWR-D-20-0391.1.

Morrison, H., 2016: Impacts of updraft size and dimensionality on the perturbation pressure and vertical velocity in cumulus convection. Part II: Comparison of theoretical and numerical solutions and fully dynamical simulations. *J. Atmos. Sci.*, **73**, 1455–1480, https://doi.org/10.1175/JAS-D-15-0041.1.

——, 2017: An analytic description of the structure and evolution of growing deep cumulus updrafts. *J. Atmos. Sci.*, **74**, 809–834, https://doi.org/10.1175/JAS-D-16-0234.1.

——, J. A. Curry, and V. I. Khvorostyanov, 2005: A new double-moment microphysics parameterization for application in cloud and climate models. Part I: Description. *J. Atmos. Sci.*, **62**, 1665–1677, https://doi.org/10.1175/JAS3446.1.

——, J. M. Peters, W. M. Hannah, A. C. Varble, and S. E. Giangrande, 2020: Thermal chains and entrainment in cumulus updrafts. Part I: Theoretical description. *J. Atmos. Sci.*, **77**, 3637–3660, https://doi.org/10.1175/JAS-D-19-0243.1.

——, ——, and S. C. Sherwood, 2021: Comparing growth rates of simulated moist and dry convective thermals. *J. Atmos. Sci.*, **78**, 797–816, https://doi.org/10.1175/JAS-D-20-0166.1.

Moser, D. H., and S. Lasher-Trapp, 2017: The influence of successive thermals on entrainment and dilution in a simulated cumulus congestus. *J. Atmos. Sci.*, **74**, 375–392, https://doi.org/10.1175/JAS-D-16-0144.1.

Mulholland, J. P., S. W. Nesbitt, R. J. Trapp, and J. M. Peters, 2020: The influence of terrain on the convective environment and associated convective morphology from an idealized modeling perspective. *J. Atmos. Sci.*, **77**, 3929–3949, https://doi.org/10.1175/JAS-D-19-0190.1.

Nelson, T. C., J. Marquis, A. Varble, and K. Friedrich, 2021: Radiosonde observations of environments supporting deep moist convection initiation during RELAMPAGO-CACTI. *Mon. Wea. Rev.*, **149**, 289–309, https://doi.org/10.1175/MWR-D-20-0148.1.

Nesbitt, S. W., and Coauthors, 2021: A storm safari in subtropical South America: Proyecto RELAMPAGO. *Bull. Amer. Meteor. Soc.*, **102**, E1621–E1644, https://doi.org/10.1175/BAMS-D-20-0029.1.

Nowotarski, C. J., P. M. Markowski, Y. P. Richardson, and G. H. Bryan, 2014: Properties of a simulated convective boundary layer in an idealized supercell thunderstorm environment. *Mon. Wea. Rev.*, **142**, 3955–3976, https://doi.org/10.1175/MWR-D-13-00349.1.

Peters, J. M., W. Hannah, and H. Morrison, 2019: The influence of vertical wind shear on moist thermals. *J. Atmos. Sci.*, **76**, 1645–1659, https://doi.org/10.1175/JAS-D-18-0296.1.

——, H. Morrison, W. M. Hannah, A. C. Varble, and S. E. Giangrande, 2020: Thermal chains and entrainment in cumulus updrafts. Part II: Analysis of idealized simulations. *J. Atmos. Sci.*, **77**, 3661–3681, https://doi.org/10.1175/JAS-D-19-0244.1.

——, ——, T. C. Nelson, J. N. Marquis, J. Mulholland, and C. J. Nowotarski, 2022a: The influence of shear on deep convection initiation. Part I: Theory. *J. Atmos. Sci.*, **79**, 1669–1690, https://doi.org/10.1175/JAS-D-21-0145.1.

——, ——, ——, ——, ——, and ——, 2022b: The influence of shear on deep convection initiation. Part II: Simulations. *J. Atmos. Sci.*, **79**, 1691–1711, https://doi.org/10.1175/JAS-D-21-0144.1.

Romps, D. M., 2010: A direct measure of entrainment. *J. Atmos. Sci.*, **67**, 1908–1927, https://doi.org/10.1175/2010JAS3371.1.

Rousseau-Rizzi, R., D. J. Kirshbaum, and M. K. Yau, 2017: Initiation of deep convection over an idealized mesoscale convergence line. *J. Atmos. Sci.*, **74**, 835–853, https://doi.org/10.1175/JAS-D-16-0221.1.

Schumacher, R. S., and Coauthors, 2021: Convective-storm environments in subtropical South America from high-frequency soundings during RELAMPAGO-CACTI. *Mon. Wea. Rev.*, **149**, 1439–1458, https://doi.org/10.1175/MWR-D-20-0293.1.

Sherwood, S. C., D. Hernandez-Deckers, M. Colin, and F. Robinson, 2013: Slippery thermals and the cumulus entrainment paradox. *J. Atmos. Sci.*, **70**, 2426–2442, https://doi.org/10.1175/JAS-D-12-0220.1.

Singh, I., S. W. Nesbitt, and C. A. Davis, 2022: Quasi-idealized numerical simulations of processes involved in orogenic convection initiation over the Sierras de Córdoba. *J. Atmos. Sci.*, **79**, 1127–1149, https://doi.org/10.1175/JAS-D-21-0007.1.

Soderholm, B., B. Ronalds, and D. J. Kirshbaum, 2014: The evolution of convective storms initiated by an isolated mountain ridge. *Mon. Wea. Rev.*, **142**, 1430–1451, https://doi.org/10.1175/MWR-D-13-00280.1.

Tian, Y., Y. Zhang, S. A. Klein, and C. Schumacher, 2021: Interpreting the diurnal cycle of clouds and precipitation in the ARM GoAmazon observations: Shallow to deep convection transition. *J. Geophys. Res. Atmos.*, **126**, e2020JD033766, https://doi.org/10.1029/2020JD033766.

Trier, S., F. Chen, and K. Manning, 2004: A study of convection initiation in a mesoscale model using high-resolution land surface initial conditions. *Mon. Wea. Rev.*, **132**, 2954–2976, https://doi.org/10.1175/MWR2839.1.

——, J. H. Marsham, C. A. Davis, and D. A. Ahijevych, 2011: Numerical simulations of the postsunrise reorganization of a nocturnal mesoscale convective system during 13 June IHOP 2002. *J. Atmos. Sci.*, **68**, 2988–3011, https://doi.org/10.1175/JAS-D-11-0112.1.

Varble, A., and Coauthors, 2014: Evaluation of cloud-resolving and limited area model intercomparison simulations using TWP-ICE observations: 1. Deep convective updraft properties. *J. Geophys. Res. Atmos.*, **119**, 13 891–13 918, https://doi.org/10.1002/2013JD021371.

——, and Coauthors, 2021: Utilizing a storm-generating hotspot to study convective cloud transitions: The CACTI experiment. *Bull. Amer. Meteor. Soc.*, **102**, E1597–E1620, https://doi.org/10.1175/BAMS-D-20-0030.1.

Wang, Q., M. Xue, and Z. Tan, 2016: Convective initiation by topographically induced convergence forcing over the Dabie Mountains on 24 June 2010. *Adv. Atmos. Sci.*, **33**, 1120–1136, https://doi.org/10.1007/s00376-016-6024-z.

Wang, S., J. C. Golaz, and Q. Wang, 2008: Effect of intense wind shear across the inversion on stratocumulus clouds. *Geophys. Res. Lett.*, **35**, L15814, https://doi.org/10.1029/2008GL033865.

——, X. Zheng, and Q. Jiang, 2012: Strongly sheared stratocumulus convection: An observationally based large-eddy simulation study. *Atmos. Chem. Phys.*, **12**, 5223–5235, https://doi.org/10.5194/acp-12-5223-2012.

Weisman, M. L., C. Davis, W. Wang, K. W. Manning, and J. B. Klemp, 2008: Experiences with 0–36-h explicit convective forecasts with the WRF-ARW model. *Wea. Forecasting*, **23**, 407–437, https://doi.org/10.1175/2007WAF2007005.1.

Wilson, J. W., and R. D. Roberts, 2006: Summary of convective storm initiation and evolution during IHOP: Observational and modeling perspective. *Mon. Wea. Rev.*, **134**, 23–47, https://doi.org/10.1175/MWR3069.1.

Xue, M., and W. J. Martin, 2006: A high-resolution modeling study of the 24 May 2002 dryline case during IHOP. Part II: Horizontal convective rolls and convective initiation. *Mon. Wea. Rev.*, **134**, 172–191, https://doi.org/10.1175/MWR3072.1.

Zhao, M., and P. H. Austin, 2005: Life cycle of numerically simulated shallow cumulus clouds. Part II: Mixing dynamics. *J. Atmos. Sci.*, **62**, 1291–1310, https://doi.org/10.1175/JAS3415.1.